Regional Difference in Dynamical Property of Sinoatrial Node Pacemaking: Role of Na^+ Channel Current

Yasutaka Kurata,* Hiroyuki Matsuda,* Ichiro Hisatome,† and Toshishige Shibamoto*
*Department of Physiology, Kanazawa Medical University, Ishikawa 920-0293, Japan, and †Division of Regenerative Medicine and Therapeutics, Tottori University Graduate School of Medical Science, Yonago 683-0826, Japan

ABSTRACT To elucidate the regional differences in sinoatrial node pacemaking mechanisms, we investigated 1), bifurcation structures during current blocks or hyperpolarization of the central and peripheral cells, 2), ionic bases of regional differences in bifurcation structures, and 3), the role of Na^+ channel current (I_{Na}) in peripheral cell pacemaking. Bifurcation analyses were performed for mathematical models of the rabbit sinoatrial node central and peripheral cells; equilibrium points, periodic orbits, and their stability were determined as functions of parameters. Structural stability against applications of acetylcholine or electrotonic modulations of the atrium was also evaluated. Blocking L-type Ca^{2+} channel current ($I_{Ca,L}$) stabilized equilibrium points and abolished pacemaking in both the center and periphery. Critical acetylcholine concentration and gap junction conductance for pacemaker cessation were higher in the periphery than in the center, being dramatically reduced by blocking I_{Na}. Under hyperpolarized conditions, blocking I_{Na}, but not eliminating $I_{Ca,L}$, abolished peripheral cell pacemaking. These results suggest that 1), $I_{Ca,L}$ is responsible for basal pacemaking in both the central and peripheral cells, 2), the peripheral cell is more robust in withstanding hyperpolarizing loads than the central cell, 3), I_{Na} improves the structural stability to hyperpolarizing loads, and 4), I_{Na}-dependent pacemaking is possible in hyperpolarized peripheral cells.

INTRODUCTION

Elucidation of the mechanisms of the sinoatrial (SA) node pacemaking is one of the most important subjects in cardiac electrophysiology. A large body of information on the ionic mechanisms of SA node pacemaking has been obtained from numerous experimental and theoretical studies (1). From the bifurcation analysis of a mathematical model for SA node primary pacemaker cells, we have elucidated the dynamical mechanisms of the natural SA node pacemaking and the roles of L-type Ca^{2+} channel current ($I_{Ca,L}$) and rapidly activating delayed-rectifier K^+ current (I_{Kr}) in basal pacemaking (2). We have suggested that 1), the instability of an equilibrium point (EP) is essentially important for pacemaker generation; 2), $I_{Ca,L}$ is responsible for EP instability and pacemaker generation, whereas I_{Kr} is not necessarily required for constructing a pacemaker cell system; and 3), I_{Kr} acts as an oscillation amplifier and frequency stabilizer as well as plays an important role in preventing bifurcation to quiescence of the system. Nevertheless, the pacemaking mechanism addressed in our previous article is for primary pacemaker cells in the central SA node. We expect that the same mechanisms underlie the pacemaking of transitional or peripheral SA node cells. However, previous reports suggest regional differences in pacemaker mechanisms, e.g., blocking $I_{Ca,L}$ abolished spontaneous activity in central SA node tissues, but not in peripheral tissues (3). In the peripheral SA node, the Na^+ channel current (I_{Na}), not present in the central SA node, might contribute to EP instability and pacemaker generation. Hyperpolarization-activated cation current (I_h) has also been suggested to play a predominant role in the subsidiary pacemaker mechanisms (4–6). Thus, regional differences in pacemaker mechanisms and roles of sarcolemmal currents, such as I_{Na} or I_h, remain to be clarified.

The aim of this study was to elucidate the regional differences in the mechanisms for basal pacemaking of SA node cells in terms of the nonlinear dynamical system theory. We particularly focused on the roles of I_{Na} in peripheral cell pacemaking, as well as the regional differences in the robustness of pacemaker activity to current blocks or hyperpolarizing loads. In previous studies, bifurcation structures (i.e., ways of changes in the number or stability of equilibrium and periodic states) of ventricular or SA node model systems were investigated for elucidating the mechanisms of normal and abnormal pacemaker activities (2,7–13). These theoretical works indicate that the initiation or cessation of pacemaker activity is considered as a bifurcation phenomenon, and that the mathematical approach—bifurcation analysis—provides a convenient way of understanding how individual currents contribute to pacemaker activities. In this study, therefore, we compared the bifurcation structures during current blocks or hyperpolarization of the central and peripheral SA node cells and also explored the ionic bases of the regional differences in bifurcation structures. Furthermore, we explored the manner in which I_{Na} contributes to the robustness of peripheral cell pacemaking and whether I_{Na}-dependent pacemaking is possible in the peripheral cell.

Local stability and bifurcation analyses were performed for the modified versions of our SA node model (14), as well as Zhang et al. models (15,16), for central and peripheral cells.

Submitted May 15, 2007, and accepted for publication March 25, 2008.

Address reprint requests to Yasutaka Kurata, Dept. of Physiology, Kanazawa Medical University, 1-1 Daigaku, Uchinada-machi, Kahoku-gun, Ishikawa 920-0293, Japan. E-mail: yasu@kanazawa-med.ac.jp

Editor: Edward H. Egelman.

0006-3495/08/07/951/27 $2.00

doi: 10.1529/biophysj.107.112854

We constructed bifurcation diagrams by calculating EPs, periodic orbits (POs), stability of EPs and POs, and bifurcation points as functions of bifurcation parameters such as the maximum current conductance. The structural stability of the model cells (robustness of pacemaker activity) was also evaluated by computing the stability and dynamics of the systems during applications of constant bias currents (I_{bias}) or acetylcholine (ACh), or during electrotonic modulations by the atrium.

A salient point of this study is that the theory of bifurcations of nonlinear dynamical systems was used to obtain significant insights into the region-dependent mechanisms of SA node pacemaking. Elucidating the regional differences in bifurcation structures of SA node cells would lead to a deeper understanding of the pacemaker mechanisms and may also provide a theoretical background for engineering a biological pacemaker (13,17,18). Definitions of the specific terms for the nonlinear dynamics and bifurcation theory are given at the end of the Theory and Methods section (see also (19–21)).

THEORY AND METHODS

Mathematical formulation

Base models for central and peripheral SA node cells

Zhang et al. (15) were the first to develop single-cell models for central and peripheral SA node cells of the rabbit that were based on the experimentally observed regional differences in action potential (AP) parameters, ionic current densities, and pharmacological responses. Their models are simplified versions that do not include intracellular Ca^{2+} dynamics or other intracellular factors. Nevertheless, we first chose to use their models, which have been corrected by Garny et al. (16), for the following reasons:

1. There was no other peripheral SA node model suitable for bifurcation analysis.
2. Their models could accurately reproduce the experimental data for the regional differences in AP dynamics and effects of various channel blockers, as summarized in Zhang et al. (15).
3. In our preliminary study, the bifurcation structures of their central cell model were essentially the same as those of our primary pacemaker model incorporating the dynamics of intracellular ion concentrations (2,14).
4. Their simple models are more suitable for bifurcation analyses than other more complex models.
5. Their cell models have been used for constructing SA node tissue models (16,22).

We found that EPs of their original models are stable, and thus they exhibit ''bistability'' (i.e., coexistence of stable steady and periodic states) under normal conditions. This implies that ''annihilation'' can easily occur in SA node cells; however, annihilation is seldom observed in SA node preparations (9). In the aspects of the nonlinear dynamics and bifurcation theory, pacemaker activity could be defined as a stable limit cycle (LC) around an unstable EP; thus, the most important dynamical property of the SA node cell system for robust pacemaking appears to be the instability of an EP (2). Other previous SA node models appear not to have a stable EP (2,23–26). Thus, we believe that EPs of SA node cell models must be unstable under normal conditions. To make the EPs unstable, therefore, the steady-state activation ($d_{L\infty}$) and inactivation ($f_{L\infty}$) curves for $I_{Ca,L}$ were positively shifted by 5 and 10 mV, respectively, with the maximum conductance ($g_{Ca,L}$) being reduced by 5%; the shifts of $d_{L\infty}$ and $f_{L\infty}$ curves were determined so as to lie within the experimental ranges as shown in Fig. 2 of Zhang et al. (15). This modification only slightly altered the AP waveforms. A complete list of the equations and standard parameter values for their models has been provided in previous articles (15,16). The formulas for the modified $I_{Ca,L}$ are given in Appendix A.

Intracellular Ca^{2+} dynamics is known to exert substantial effects on the dynamics of pacemaker cells and may also significantly affect the bifurcation structures of SA node cells. Therefore, we also used models that incorporated intracellular Ca^{2+} dynamics. On the basis of the Zhang et al. models (15) and related experimental data, we developed the central and peripheral versions of our SA node model (14). Although the expressions for individual components of our modified models (referred to as the Kurata et al. models) are essentially the same as in the previous article (14), the original formulas for I_{Na} and I_h were replaced by those of the Zhang et al. models for the following reasons: 1), the I_{Na} formulas of the Zhang et al. model yielded better fits to the experimental data for SA node I_{Na} kinetics (27,28), and 2), voltage dependence of the original formula for I_h activation (y^2) was so steep that I_h became too large for the peripheral cell model and yielded irregular dynamics. Standard parameter values for the Kurata et al. models are provided in Table 1. Dynamics of the Kurata et al. models, as well as the Zhang et al. models, with the standard parameter values are shown in Appendix A (see Fig. 17).

In our original or other SA node models, the contribution of sarcoplasmic reticulum (SR) Ca^{2+} cycling to pacemaker activity was small; the suppression of SR Ca^{2+} release did not slow pacemaking as dramatically as did the application of ryanodine or BAPTA in experiments (see Table 4 of Kurata et al. (14)). To examine how SR Ca^{2+} release affects the stability, dynamics, and bifurcation of SA node cells, we developed the modified versions of our SA node model for which SR Ca^{2+} cycling was enhanced by increasing the rate constants of Ca^{2+} uptake (P_{up}) and release (P_{rel}). The central cell model with increased P_{up} and P_{rel} could exhibit a 68.1–112.2% increase in CL on minimizing SR Ca^{2+} release, whereas a peripheral version of such a large response could not be developed, probably because of the presence of large I_{Na} (data not shown). Bifurcation structures of our original model and the modified models with enhanced SR Ca^{2+} cycling were essentially the same (data not shown). Thus, only the data from the models of the medium response (yielding 11.8–23.7% increases in CL) are shown in this article.

The standard models for the normal pacemaker activity include 13–14 membrane current components. The time-dependent change in the membrane potential (V_S) is described by

$$dV_S/dt = -(I_{Ca,L} + I_{Ca,T} + I_{Na} + I_h + I_{st} + I_{Kr} + I_{Ks} + I_{to} + I_{sus} + I_{b,Na} + I_{b,Ca} + I_{b,K} + I_{NaK} + I_{NaCa})/C_S, \quad (1)$$

where $I_{Ca,L}$ and $I_{Ca,T}$ represent the L-type and T-type Ca^{2+} channel currents, respectively. The rapid and slow components of the delayed-rectifier K^+ currents are denoted as I_{Kr} and I_{Ks}, respectively. The membrane current system also includes I_{Na}, I_h, the sustained inward current (I_{st}), four AP-sensitive currents consisting of transient (I_{to}) and sustained (I_{sus}) components, background currents carried by Na^+ ($I_{b,Na}$), Ca^{2+} ($I_{b,Ca}$) and K^+ ($I_{b,K}$), Na^+-K^+ pump current (I_{NaK}), and Na^+/Ca^{2+} exchanger current (I_{NaCa}). All the currents charge the membrane capacitance (C_S).

Incorporation of ACh effects on ionic currents

To investigate the bifurcation structure of the model cells during applications of ACh, we incorporated the formulas of Dokos et al. (29) or Zhang et al. (30) for the muscarinic K^+ channel current ($I_{K,ACh}$), as well as for the modifications of $I_{Ca,L}$ and I_h by ACh, into the base models. Both the formula sets yielded qualitatively the same results; thus, only the results obtained with the formulas of Dokos et al. (29) are shown. It is unknown whether the density of the muscarinic K^+ channel varies between the center and periphery of the SA node, whereas the density of the muscarinic M_2 receptor as well as vagal innervation may be greater in the center than in the periphery (31,32). In this study, therefore, it was assumed that the $I_{K,ACh}$ density is the same in central and peripheral cells, as in Zhang et al. (30). Sensitivities to ACh of $I_{K,ACh}$, $I_{Ca,L}$, and I_h were also assumed to be independent of the regions. The ex-

TABLE 1 Standard parameter values for the original and modified Kurata et al. models

Parameters	Units	Original central*	Modified central	Modified peripheral
C_m	pF	32	20	65
V_{cell}	pL	3.5186	2.19911	7.147123
V_{sub}	pL	0.0351	0.021936	0.0712925
V_i	pL	1.5835	0.98965	3.216384
V_{rel}	pL	0.0042	0.0026389	0.00857654
V_{up}	pL	0.0408	0.0255097	0.0829066
$[K^+]_o$	mM	5.4	5.4	5.4
$[K^+]_i$	mM	Variable	140	140
$g_{Ca,L}$	nS/pF	0.58	0.58	1.6008
g_{Kr}	nS/pF	$0.025 \times [K^+]_o^{0.59}$	$0.025 \times [K^+]_o^{0.59}$	$0.09255 \times [K^+]_o^{0.59}$
g_{Ks}	nS/pF	0.0259	0.0259	0.0958818
g_{to}	nS/pF	0.18	0.18	0.4194
g_{sus}	nS/pF	0.02	0.02	0.0466
g_{Na}†		0	*0*	*1.204×10^{-15}*
$g_{Ca,T}$	nS/pF	0.458	0.458	0.458
g_h†	nS/pF	0.375	*0.05465*	*0.1565*
g_{st}	nS/pF	0.015	0.0075	0
$g_{Na,b}$	nS/pF	0.0054	0.0054	0.0093312
$g_{K,ACh}$	pA × mM^{-1} × pF^{-1}	$0.0011 \times [K^+]_o^{0.41}$	$0.0011 \times [K^+]_o^{0.41}$	$0.0011 \times [K^+]_o^{0.41}$
I_{NaKmax}	pA/pF	3.6	3.6	9.72‡
k_{NaCa}	pF^{-1}	125	125	187.5‡
$T_{dif,Ca}$	ms	0.04	0.01	0.01
P_{rel}	ms^{-1}	0.5	1.25	2.50
P_{up}	mM × ms^{-1}	0.005	0.01	0.02
$k\tau_q$§		1	0.670	0.670
$k\tau_r$§		1	0.303	0.303

*Parameter values used for the original Kurata et al. model (14) are given for comparison.
†Values are shown in *italic*, because the formulas used in this study are different from those of the original model and thus direct comparison is impossible.
‡Higher activities of Na^+-K^+ pump and Na^+/Ca^{2+} exchanger were required to counteract the increased Ca^{2+} and Na^+ influx via Na^+ and Ca^{2+} channels.
§Scaling factors for the activation and inactivation time constants of I_{to} and I_{sus}, which were determined for the peripheral model to reproduce the AP waveform experimentally observed in the periphery of SA node tissues (15).

pressions for these currents with the ACh modifications of Dokos et al. (29) are given in Appendix A.

Formulation of a coupled-cell model

To investigate the electrotonic influences of atrial myocytes on stability and dynamics of SA node cells, we used a coupled-cell model as introduced by Watanabe et al. (33). According to their method, a SA node cell was connected to a passive membrane model (resistance-capacitance (R-C) circuit) for an atrial myocyte via the gap junction conductance (G_C) of 0–20 nS. We used an atrial membrane capacitance (C_A) of 51 pF and an atrial membrane resistance (R_A) of 0.22 GOhm, as in Watanabe et al. (33), for the central cell ($C_S = 20$ pF). For the peripheral cell with a larger capacitance ($C_S = 65$ pF), the C_A and R_A values were scaled by multiplying 3.25 and 3.25^{-1}, respectively, to yield the same capacitance ratio (C_S/C_A) for the peripheral cell as for the central cell. An offset voltage, corresponding to a resting potential of the atrial myocyte, was set equal to −80 mV.

Time-dependent changes in the membrane potentials of the SA node cell (V_S) and atrial myocyte (V_A) were calculated by the equations

$$dV_S/dt = -(I_{total} + I_C/C_S) \quad (2)$$

$$dV_A/dt = (I_C - I_A)/C_A \quad (3)$$

$$I_C = G_C(V_S - V_A) \quad (4)$$

$$I_A = (V_A + 80)/R_A, \quad (5)$$

where I_{total} and I_A represent the sum of sarcolemmal ionic currents in the SA node cell (pA/pF) and the atrial membrane current (pA), respectively. I_C denotes the gap junction current (pA).

Bifurcation analysis

The model cells are 15- or 26-order autonomous continuous-time dynamical systems, each of which is described as a set of 15 or 26 first-order, nonlinear ordinary differential equations. Dynamical properties and bifurcation structures of a model cell system were determined by analytically and numerically handling the differential equations. Numerical computations were performed with MATLAB 7 for Windows XP (The MathWorks, Natick, MA) on Workstation HP xw9300 (Hewlett-Packard, Tokyo, Japan) and CELSIUS X630 (Fujitsu, Tokyo, Japan).

Locating EPs and LCs

In the model cell systems, 15 or 26 state variables define a 15- or 26-dimensional state point in the 15- or 26-dimensional state space. We calculated EPs and LCs (isolated POs) in the state space. An EP was determined as a point at which the vector field vanishes. A steady-state value of the state variable V_S (for $dV_S/dt = 0$) was calculated by the Newton-Raphson algorithm, practically with a nonlinear equation solver (fsolve) available in MATLAB 7 (optimization toolbox); then, steady-state values of the gating variables for individual currents were computed. A stable LC was located by the brute-force approach or autonomous shooting method (20) using the numerical algorithms available as MATLAB ODE solvers, i.e., 1), a variable time-step numerical differentiation approach selected for its suitability to stiff systems (ode15s) and 2), a fourth-order adaptive-step Runge-Kutta algorithm (ode45). When a stable LC appeared, the AP amplitude (APA) as a voltage difference between the local potential minimum (V_{min}) and maximum (V_{max}), as well as the cycle length (CL), was determined for each calculation of a cycle. Numerical integration was continued until the differences in both APA and CL between the newly calculated cycle and the preceding one became

$<1 \times 10^{-3}$ of the preceding APA and CL values. To locate an unstable LC, we used CL_MATCONT, a continuation toolbox for MATLAB (34).

Constructing one-parameter bifurcation diagrams

To examine how the stability and dynamics of the model cells alter with changes in bifurcation parameters, we constructed one-parameter bifurcation diagrams in which values of a state variable at EPs and extrema of LCs are plotted as functions of the bifurcation parameters. Bifurcation parameters chosen in this study include 1), the maximum conductance of $I_{Ca,L}$ ($g_{Ca,L}$), I_{Kr} (g_{Kr}), I_{Na} (g_{Na}), I_h (g_h), and $I_{Ca,T}$ ($g_{Ca,T}$); 2), amplitude of I_{bias}; 3), ACh concentration ([ACh]); and 4), G_C. The maximum conductance is expressed as normalized values, i.e., ratios to the control value.

A single bifurcation parameter was systematically changed while keeping all other parameters at their standard values. The steady-state membrane potential (V_E) at EPs (steady-state branches) and local potential extrema (V_{min}, V_{max}) of LCs (periodic branches), as well as the CL of LCs, were determined and plotted for each value of the bifurcation parameter. When periodic behavior was irregular, model cell dynamics were computed for 60 s; all potential extrema and CL values sampled during the last 10 s were then plotted in the diagrams.

Detecting codimension-one bifurcations (determination of EP and LC stabilities)

The critical parameter value (bifurcation point) at which a codimension-one bifurcation occurs was determined by evaluating the existence and stability of EPs and LCs at each value of a relevant parameter (one-parameter bifurcation analysis). The asymptotic stability of an EP was determined by computing eigenvalues of a Jacobian matrix derived from the linearization of the nonlinear systems around the EP (for details, see Appendix B). The stability of an LC was determined by its characteristic multipliers, which were calculated as eigenvalues of the solution of the variational equation (for more details, see (9,12,20)).

The Hopf bifurcation point at which the stability of an EP reverses was determined by the stability analysis. The saddle-node (SN) bifurcation point at which two EPs coalesce and disappear was also detected as a point at which the steady-state current-voltage (I/V) curve and zero-current axis come in contact with each other. Moreover, the saddle-node, period-doubling, and Neimark-Sacker bifurcations were detected for LCs (for details, see ''Definitions of Terms'' at the end of this section and also (9,21)).

Constructing two-parameter bifurcation diagrams

We further constructed two-parameter bifurcation diagrams in which the path of codimension-one bifurcation determined by the one-parameter bifurcation analysis is traced in a parameter plane. The primary parameter was systematically changed with the secondary parameter fixed at a constant value. The critical value of the primary parameter at which Hopf or saddle-node bifurcations occur on the steady-state branch was determined for various different values of the secondary parameter. Bifurcation values for the primary parameter were plotted as a function of the secondary parameter. Codimension-two saddle-node bifurcation at which two loci of codimension-one (Hopf) bifurcation points coalesce and disappear was detected.

Definition and evaluation of structural stability

We also evaluated the structural stability of SA node cells, which is defined as the robustness of pacemaker activity to various interventions or modifications that may cause a bifurcation to quiescence or irregular dynamics (for details, see Kurata et al. (2)). In this study, we tested the structural stability against applications of hyperpolarizing (or depolarizing) I_{bias} or ACh and against electrotonic loads of an adjacent atrial myocyte.

The manner of evaluating the structural stability to I_{bias} is essentially the same as described in our previous articles (2,13). Changes in V_E and its stability during I_{bias} applications were depicted as the I_{bias}-V_E curve (for more details, see Fig. 4 in the Results section; see also Fig. 1 of Kurata et al. (2)). Hopf and saddle-node bifurcation points in the I_{bias}-V_E curve were determined as functions of bifurcation parameters and plotted on both the potential and current coordinates. Changes in EPs, LC dynamics, and their stability were also determined with increasing [ACh] or G_C; the Hopf bifurcation for EP stabilization, as well as the saddle-node, period-doubling, or Neimark-Sacker bifurcation causing cessation or destabilization of LCs, were detected.

In the unstable I_{bias}, [ACh] or G_C region, a system has an unstable EP only (no stable EP), generally exhibiting robust pacemaking (stable LCs) without annihilation. When the system removes to the stable I_{bias}, [ACh] or G_C region with a stable EP, it would, however, come to a rest at the stable EP via gradual decline of LCs, annihilation, or irregular dynamics (9). Thus, the larger the unstable I_{bias}, [ACh], or G_C range is, the more structurally stable the pacemaker system is.

Definitions of terms specific to nonlinear dynamics and bifurcation theory

Autonomous system

An nth-order autonomous continuous-time dynamical system is defined by the state equation, $d\mathbf{x}/dt = \mathbf{f}(\mathbf{x})$, where the vector field $\mathbf{f}$ does not depend on time but depends only on the state variable $\mathbf{x}$ (20). A dynamical system is nonautonomous when the vector field $\mathbf{f}$ explicitly contains time $\mathbf{t}$.

Limit set

The set of points in state space that a trajectory repeatedly visits in autonomous systems.

Equilibrium point

A time-independent steady-state point at which the vector field vanishes (i.e., $d\mathbf{x}/dt = 0$) in the state space of an autonomous system, constructing the steady-state branch in one-parameter bifurcation diagrams. This state point corresponds to the zero-current crossing in the steady-state I/V curve, i.e., a quiescent state of a cell if it is stable.

Periodic orbit

A closed trajectory in the state space of a system, constructing the periodic branch in one-parameter bifurcation diagrams.

Limit cycle

An isolated periodic limit set onto which a trajectory is asymptotically attracted in an autonomous system. A stable LC corresponds to an oscillatory state—i.e., pacemaker activity—of a cell.

Bifurcation

A qualitative change in a limit set (i.e., in a solution of ordinary differential equations) caused by altering parameters, *e.g.*, a change in the number of EPs or LCs, a change in the stability of an EP or LC, and a transition from a periodic to quiescent state. Bifurcation phenomena that can be observed in cardiac cells include a cessation or generation of pacemaker activity and occurrence of irregular dynamics such as skipped-beat runs (9).

Hopf bifurcation

This is a bifurcation at which the stability of an EP reverses with emergence or disappearance of a LC, occurring when the eigenvalues of a Jacobian matrix for the EP have a single complex conjugate pair and its real part reverses the sign through zero. It is supercritical when a stable EP becomes unstable with the emergence of a stable LC; it is subcritical when an unstable EP becomes stable with emergence of an unstable LC (21).

Saddle-node bifurcation

This is a bifurcation at which two EPs (steady-state branches) or two periodic solutions (periodic branches) coalesce and disappear, also called a fold or limit point bifurcation. The saddle-node bifurcation of EPs occurs when one of eigenvalues of a Jacobian matrix is zero; that of LCs occurs when one of characteristic multipliers becomes >1.

Period-doubling bifurcation

This is a bifurcation at which a stable period-K solution becomes unstable and spawns a stable period-2K solution (20), also referred to as a flip bifurcation. This occurs when one of characteristic multipliers becomes <-1.

Neimark-Sacker bifurcation

This is a bifurcation at which a stable LC becomes unstable with emergence of torus trajectories; it is thus also called a torus bifurcation. This bifurcation occurs when a complex conjugate pair of characteristic multipliers comes outside of a unit circle in the complex plane.

Codimension

The codimension of a bifurcation is the minimum dimension of the parameter space in which the bifurcation may occur in a persistent way (19,35). In other words, the codimension is the number of independent conditions determining the bifurcation (21). A bifurcation with codimension 1 is a point in one-parameter bifurcation diagrams or a line in two-parameter bifurcation diagrams, whereas a bifurcation with codimension 2 is a point in the two-parameter space.

Bistability

This means the coexistence of two stable structures in the phase space of a system. In the region of bistability, two stable EPs or stable LCs coexist, or a stable LC coexists with a stable EP (7,9,10,12). Thus, the system has two stable solutions at the same time in the bistable zone. Bistability links to the transition between two stable states; e.g., annihilation (transition from LC to EP) and single-pulse triggering (transition from EP to LC) could be achieved.

Annihilation

Permanent stable extinction of spontaneous activity, which depends upon the polarity, timing, and magnitude of the applied stimuli (9,10,12).

RESULTS

Regional differences in bifurcation structures of SA node cells

To elucidate the regional differences in pacemaker mechanisms and robustness of pacemaker activity, we compared the stability, dynamics, and bifurcation structures of the central and peripheral cells during sarcolemmal ionic current blocks or hyperpolarization.

Effects of blocking ionic currents or SR Ca^{2+} release on pacemaker activities

We first simulated the effects of blocking sarcolemmal ionic currents or SR Ca^{2+} release current (I_{rel}) on pacemaker activity by decreasing the current conductance. Dynamic behaviors of the central and peripheral cell models with normal and decreased conductance are shown in Fig. 1. When $I_{Ca,L}$ or I_{Kr} was completely blocked, spontaneous activity ceased in both the central and peripheral cells. In contrast, the elimination of I_{Na}, I_h, or $I_{Ca,T}$, although slowing pacemaking, did not abolish pacemaker activity of either the central or peripheral cell. These simulated results are consistent with those shown in the original article of Zhang et al. (15), except that peripheral cell pacemaking ceased during the $I_{Ca,L}$ block. Decreasing I_{NaCa} also abolished spontaneous oscillations in the Kurata et al. models, although it did not do so in the Zhang et al. models. This is a consequence of the Ca^{2+}-dependent inactivation of $I_{Ca,L}$ under Ca^{2+} overload conditions because pacemaker activities of the Kurata et al. models did not cease during the inhibition of I_{NaCa} when Ca^{2+}-dependent inactivation of $I_{Ca,L}$ was removed or when intracellular Ca^{2+} concentrations were fixed (data not shown). In the Kurata et al. models, spontaneous oscillations were slowed but not abolished by decreasing I_{rel}.

Comparison of bifurcation structures during inhibition of $I_{Ca,L}$ or I_{Kr}

Blocking $I_{Ca,L}$ or I_{Kr}, but not blocking other currents, abolished pacemaker activity in both the central and peripheral cells. Thus, we explored the stability, dynamics, and bifurcation structures of the model cells during the inhibition of $I_{Ca,L}$ or I_{Kr}. Figs. 2 and 3 show the bifurcation diagrams constructed for $g_{Ca,L}$ and g_{Kr}, respectively, depicting the V_E at EPs (steady-state branch), local potential extrema of LCs (periodic branches), and the CL of LCs as functions of $g_{Ca,L}$ or g_{Kr}.

During the block of $I_{Ca,L}$ (decrease in $g_{Ca,L}$), the EP was stabilized via a Hopf bifurcation with emergence of an unstable LC or disappearance of a stable LC. In the Zhang et al. models and Kurata et al. peripheral model, stable and unstable LCs (periodic branches) abruptly disappeared via a saddle-node bifurcation, with the cells coming to quiescence. In the Kurata et al. central model, irregular dynamics emerged via a Neimark-Sacker bifurcation before cessation of spontaneous activity. It should be noted that the critical $g_{Ca,L}$ values at the bifurcation points were smaller in the peripheral cell than in the central cell and that the Zhang et al. models and Kurata et al. peripheral model exhibited bistability, i.e., the coexistence of a stable EP and a stable LC.

The block of I_{Kr} (decrease in g_{Kr}) also caused EP stabilization via a Hopf bifurcation. Stable and unstable LCs of the Zhang et al. central model abruptly vanished via a saddle-node bifurcation, whereas the stable LC of the other model cells gradually contracted in size and collapsed at the Hopf bifurcation point. The critical g_{Kr} value at which the saddle-node or Hopf bifurcation to quiescence occurs was lower in the peripheral cell than in the central cell.

Influences of blocking $I_{Ca,L}$ or I_{Kr} on stability and bifurcations during I_{bias} applications

We also examined the influences of blocking $I_{Ca,L}$ or I_{Kr} on bifurcation structures (stability, dynamics, and bifurcations) during I_{bias} applications of the model cells. In Fig. 4, changes

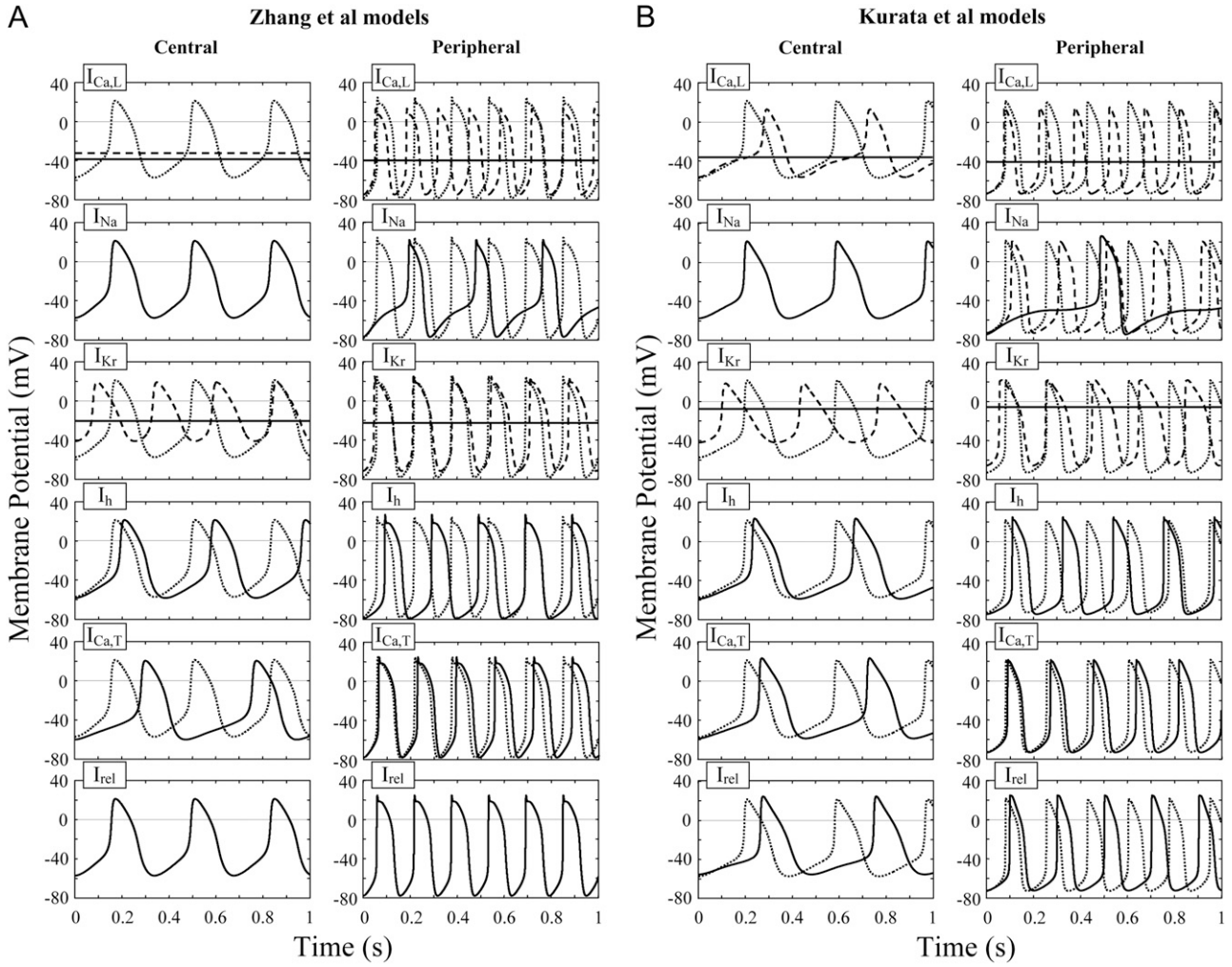

FIGURE 1 Simulated effects of blocking individual sarcolemmal currents or SR Ca^{2+} release on pacemaker activity of the Zhang et al. (*A*) and Kurata et al. (*B*) models for the central and peripheral cells. Membrane potential behaviors on decreasing one of $I_{Ca,L}$, I_{Na}, I_{Kr}, I_h, $I_{Ca,T}$, and the SR Ca^{2+} release current I_{rel} (from *top* to *bottom*) are shown. Effects of the complete block of each current (*solid lines*) and 50% block of $I_{Ca,L}$, I_{Na}, or I_{Kr} (*dashed lines*) were tested. The SR Ca^{2+} release rate (P_{rel}) was reduced to 1% of the control value. Control APs are superimposed in each panel (*dotted lines*). Differential equations of the model systems were numerically solved for 11 s (*A*) or 301 s (*B*), with an initial condition appropriate to an EP and a 1-ms stimulus of 1 pA/pF; the membrane potential behaviors during the last 1 s (starting from a maximum diastolic potential) were depicted.

in V_E and its stability during I_{bias} applications are depicted as the I_{bias}-V_E curves for the normal, $I_{Ca,L}$-removed and I_{Kr}-removed versions of the Kurata et al. models. The control EP (V_E) at $I_{bias} = 0$ is unstable in the normal systems because two eigenvalues of a Jacobian matrix for the EP are positive real numbers; in contrast, those in the $I_{Ca,L}$- and I_{Kr}-removed systems are stable because all the real parts of eigenvalues (Re[λ]) are negative. There are 2–4 Hopf bifurcation points (labeled as H1–H4), where real parts of a pair of the complex conjugate eigenvalues go through zero and reverse their sign. In the whole interval between H1 and H2, the systems have no stable EP but have only one unstable EP, generating LC oscillations (Fig. 5). Saddle-node bifurcations at which multiple EPs emerge occurred in the I_{Kr}-removed systems.

Figs. 6 and 7 show the displacement of Hopf and saddle-node bifurcation points in the I_{bias}-V_E curve, as well as the shift in the control V_E at $I_{bias} = 0$ (V_0), with decreases in $g_{Ca,L}$ and g_{Kr}, respectively. Bifurcation points were plotted as functions of $g_{Ca,L}$ or g_{Kr} on both the potential (V_E) and current (I_{bias}) coordinates. In the central cells, the unstable V_E and I_{bias} regions between H1 and H2 shrunk with decreasing $g_{Ca,L}$, and finally disappeared via a codimension-two saddle-node bifurcation. In contrast, the unstable regions of the peripheral cells did not vanish even when $I_{Ca,L}$ was completely blocked. Reducing g_{Kr} did not significantly shrink the unstable V_E range in either the central or peripheral cells. The unstable I_{bias} regions did not disappear even when I_{Kr} was removed. The $I_{Ca,L}$-removed peripheral cells as well as the I_{Kr}-removed cells—quiescent at $I_{bias} = 0$—resumed spontaneous oscillations when an EP was destabilized by applications of hyperpolarizing I_{bias} (see Fig. 5).

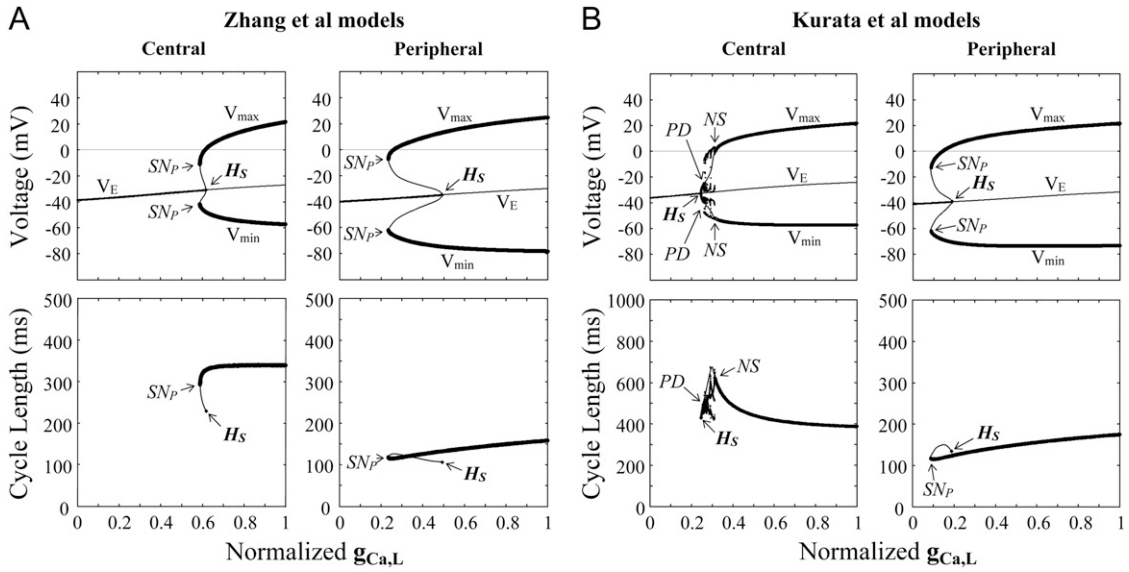

FIGURE 2 Effects of reducing $g_{Ca,L}$ on the EP stability and oscillation dynamics of the Zhang et al. (*A*) and Kurata et al. (*B*) models for central and peripheral cells. One-parameter bifurcation diagrams for $g_{Ca,L}$ with the steady-state branch as a locus of V_E and the periodic branches as the potential extrema of LCs (V_{min}, V_{max}) are shown (*top*); the CL of LCs is also plotted as a function of $g_{Ca,L}$ (*bottom*). The steady-state and periodic branches consist of the stable (*thick lines*) and unstable (*thin lines*) segments. The normalized $g_{Ca,L}$ value was reduced at an interval of 0.001 for calculations of EPs and stable LCs. The points of Hopf bifurcation of EPs, saddle-node bifurcation of LCs, period-doubling bifurcation of LCs, and Neimark-Sacker bifurcation of LCs are located, as labeled H_S, SN_P, *PD*, and *NS*, respectively: (*A*) H_S at $g_{Ca,L} = 0.6178$ (*central*) and 0.4912 (*peripheral*); SN_P at $g_{Ca,L} = 0.5890$ (*central*) and 0.2337 (*peripheral*). (*B*) H_S at $g_{Ca,L} = 0.2457$ (*central*) and 0.1891 (*peripheral*); SN_P at $g_{Ca,L} = 0.085$ (*peripheral*); *PD* at $g_{Ca,L} = 0.257$ (*central*); and *NS* at $g_{Ca,L} = 0.312$ (*central*).

Bifurcation structures during ACh applications or electrotonic modulations

We further examined the regional differences in the structural stability against hyperpolarizing loads by comparing the bifurcation structures of the central and peripheral cells during ACh applications or electrotonic modulations. Figs. 8 and 9 show the stability, dynamics, and bifurcations of the model cells as functions of [ACh] and G_C, respectively.

During increases in [ACh], EPs of the central and peripheral cells were destabilized via Hopf bifurcations. In the Zhang et al. central model, a stable LC abruptly vanished via a saddle-node bifurcation, with the cell coming to a rest;

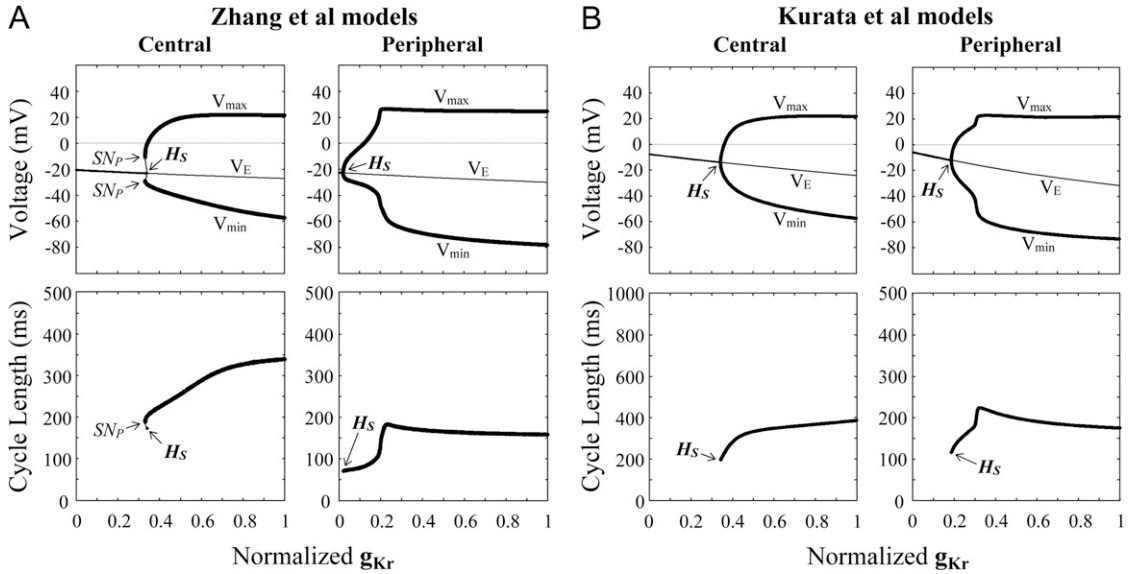

FIGURE 3 Effects of reducing g_{Kr} on the EP stability and oscillation dynamics of the Zhang et al. (*A*) and Kurata et al. (*B*) models. One-parameter bifurcation diagrams for g_{Kr} with the steady-state branch (V_E) and the periodic branches (V_{min}, V_{max}) are shown (*top*); the CL of LCs is also plotted as a function of g_{Kr} (*bottom*). The normalized g_{Kr} value was reduced at an interval of 0.001 for calculations of EPs and stable LCs. The points of Hopf bifurcation of EPs (H_S) and saddle-node bifurcation of LCs (SN_P) are located: (*A*) H_S at $g_{Kr} = 0.3384$ (*central*) and 0.0228 (*peripheral*); SN_P at $g_{Kr} = 0.3298$ (*central*). (*B*) H_S at $g_{Kr} = 0.3440$ (*central*) and 0.1867 (*peripheral*).

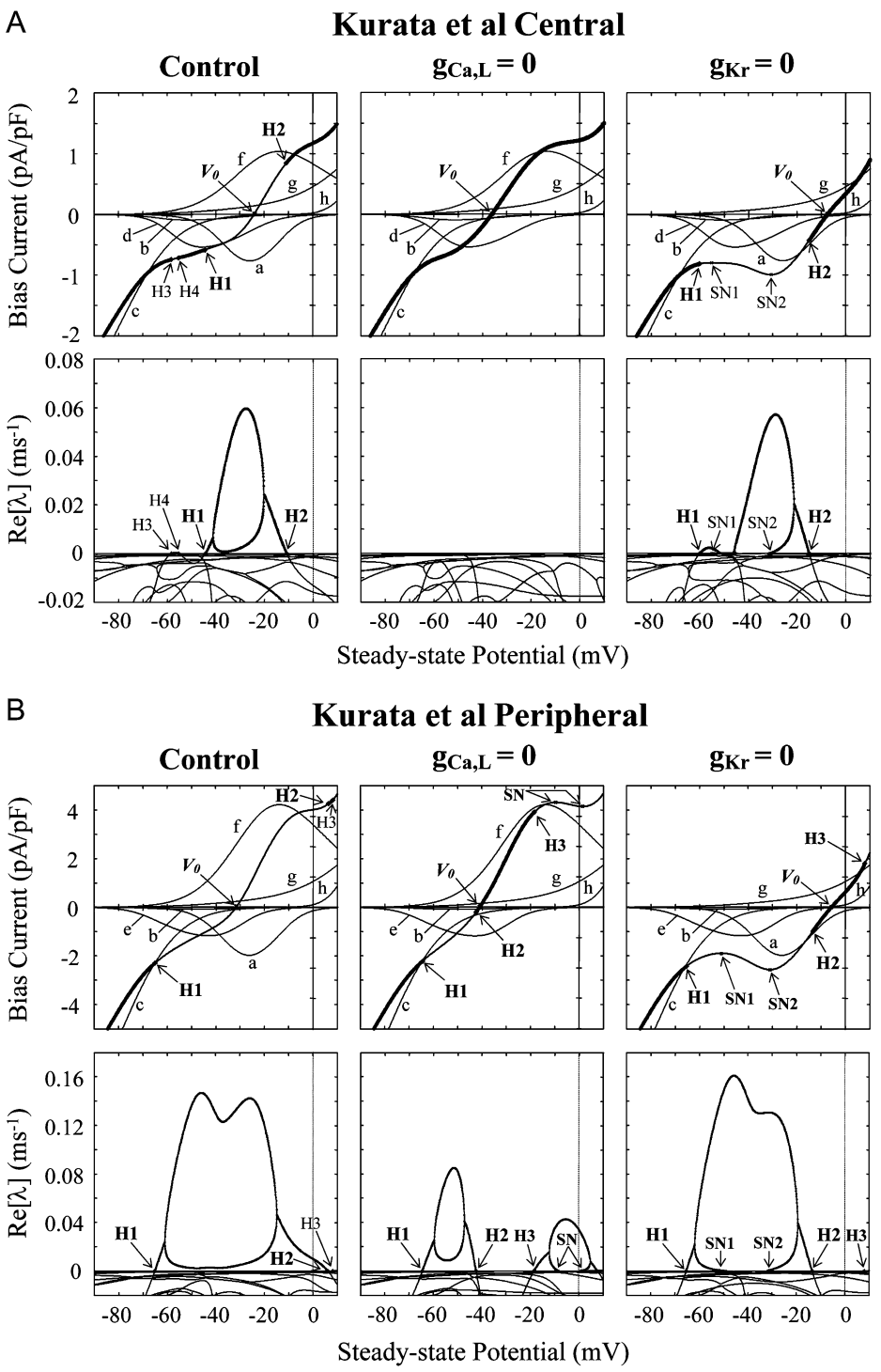

FIGURE 4 Changes in EPs and their stability during I_{bias} applications of the normal (*control*), $I_{Ca,L}$-removed ($g_{Ca,L} = 0$), and I_{Kr}-removed ($g_{Kr} = 0$) versions of the Kurata et al. central (*A*) and peripheral (B) models. Shown are the I_{bias}-V_E curves illustrating how V_E and its stability changed when I_{bias} was applied (*top*). V_E was systematically changed by applying hyperpolarizing (negative) or depolarizing (positive) I_{bias} of various amplitudes; the resulting relationship between V_E (abscissa) and I_{bias} amplitude (ordinate) is depicted. Stability of EPs was evaluated by the stability analysis based on the linear stability theory (see Appendix B); real parts of eigenvalues (Re[λ]) of a Jacobian matrix for each EP (V_E) representing the rate constants (ms^{-1}) of a system to be attracted to or go away from an EP are shown (*bottom*). In the I_{bias}-V_E curve, the segments of thin lines designate the loci of unstable EPs with two positive Re[λ] values; those of thick lines are the stable EPs for which Re[λ] values are all negative. There are 2–4 Hopf bifurcation points (*H1–H4*), corresponding to the zero crossings of Re[λ]. Saddle-node bifurcation points are also located (labeled *SN*). Individual time-dependent current components in steady state are superimposed to show the contribution of each current to the stability of EPs: *a*, $I_{Ca,L}$; *b*, $I_{Ca,T}$; *c*, I_h; *d*, I_{st}; *e*, I_{Na}; *f*, I_{Kr}; *g*, $I_{to} + I_{sus}$; and *h*, I_{Ks}.

in their peripheral model and Kurata et al. models, an LC became unstable via a period-doubling bifurcation with emergence of irregular dynamics between the period-doubling and Hopf bifurcation points. Destabilization of EPs via Hopf bifurcations was also observed during increases of G_C in the coupled-cell models. A stable LC of the Zhang et al. central cell abruptly vanished via a saddle-node bifurcation leading to quiescence; in their peripheral model and Kurata et al. models, an LC became unstable via a saddle-node, period-doubling, or Neimark-Sacker bifurcation with emergence of irregular dynamics. The critical [ACh] and G_C values at the bifurcations to quiescence were much greater for the peripheral cell than for the central cell.

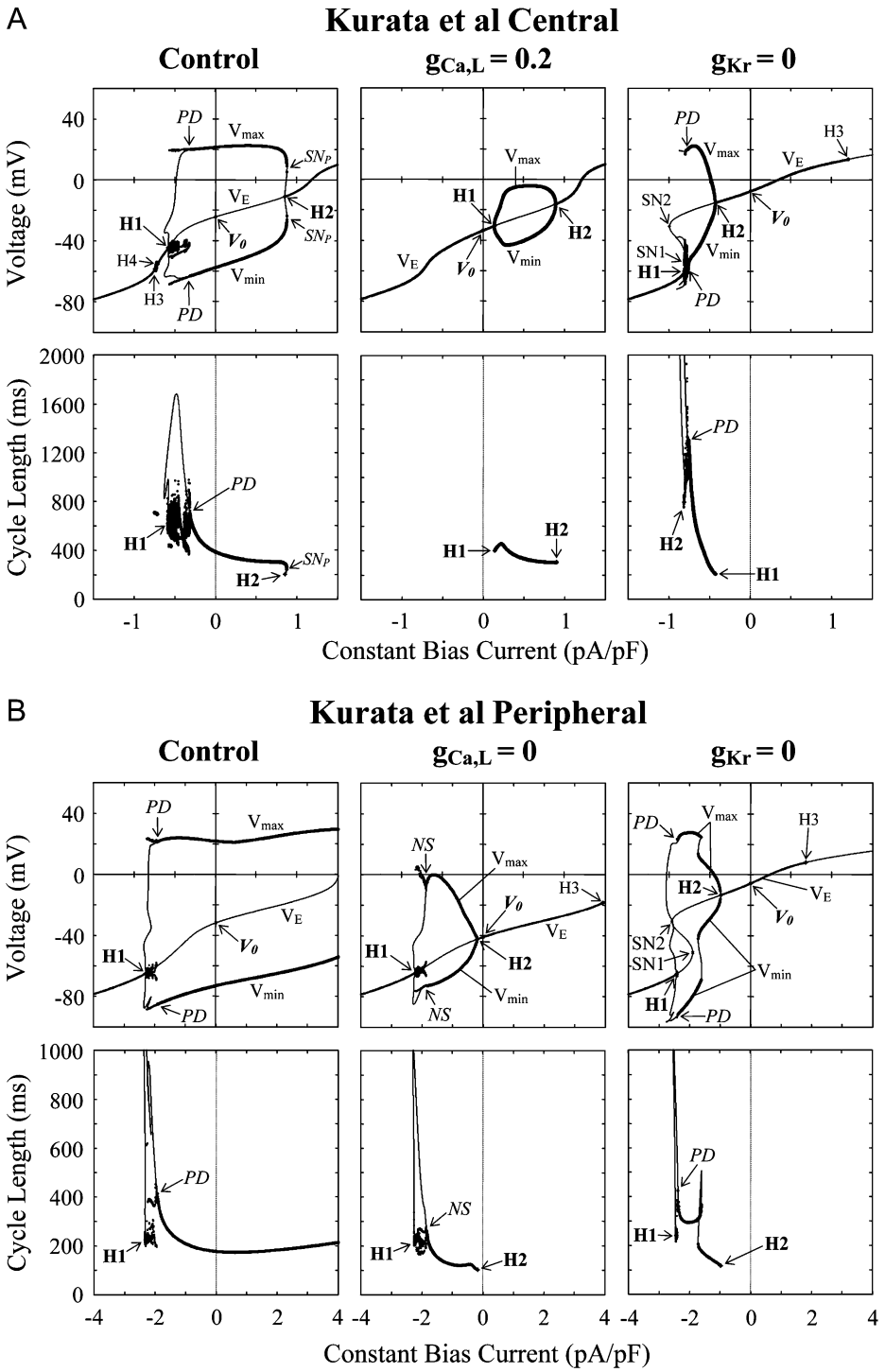

FIGURE 5 Oscillation dynamics during I_{bias} applications of the normal (*control*), $I_{Ca,L}$-reduced ($g_{Ca,L}$ = 0.2 or 0), and I_{Kr}-removed (g_{Kr} = 0) versions of the Kurata et al. central (*A*) and peripheral (*B*) models. A bifurcation diagram for I_{bias} with the steady-state (V_E) and stable periodic (V_{min}, V_{max}) branches is shown; CL is also plotted against I_{bias}. Various amplitudes of hyperpolarizing (negative) or depolarizing (positive) I_{bias} were applied at an interval of 0.001 pA/pF. Hopf (*H1–H3*) or saddle-node (*SN1*, *SN2*) bifurcation of EPs, and saddle-node (SN_P), period-doubling (*PD*), or Neimark-Sacker (*NS*) bifurcation of LCs are located.

Ionic bases of regional differences in bifurcation structures

Our results above suggest certain regional differences in bifurcation structures that can be summarized as follows: 1), the unstable V_E (EP) region determined by applications of hyperpolarizing I_{bias} was abolished by blocking $I_{Ca,L}$ in the central cells but not in the peripheral cells (Fig. 6), and 2), the critical [ACh] and G_C values for the stabilization of EPs and abolition of stable LCs were much greater in the periphery than in the center (Figs. 8 and 9). To elucidate the ionic bases of these regional differences, we further explored how blocking individual sarcolemmal currents affects EP stability, oscillation dynamics, and bifurcation structures of the model systems. We particularly focused on the contributions of I_{Na} and I_h, the densities of which are much greater in the periphery than in the center.

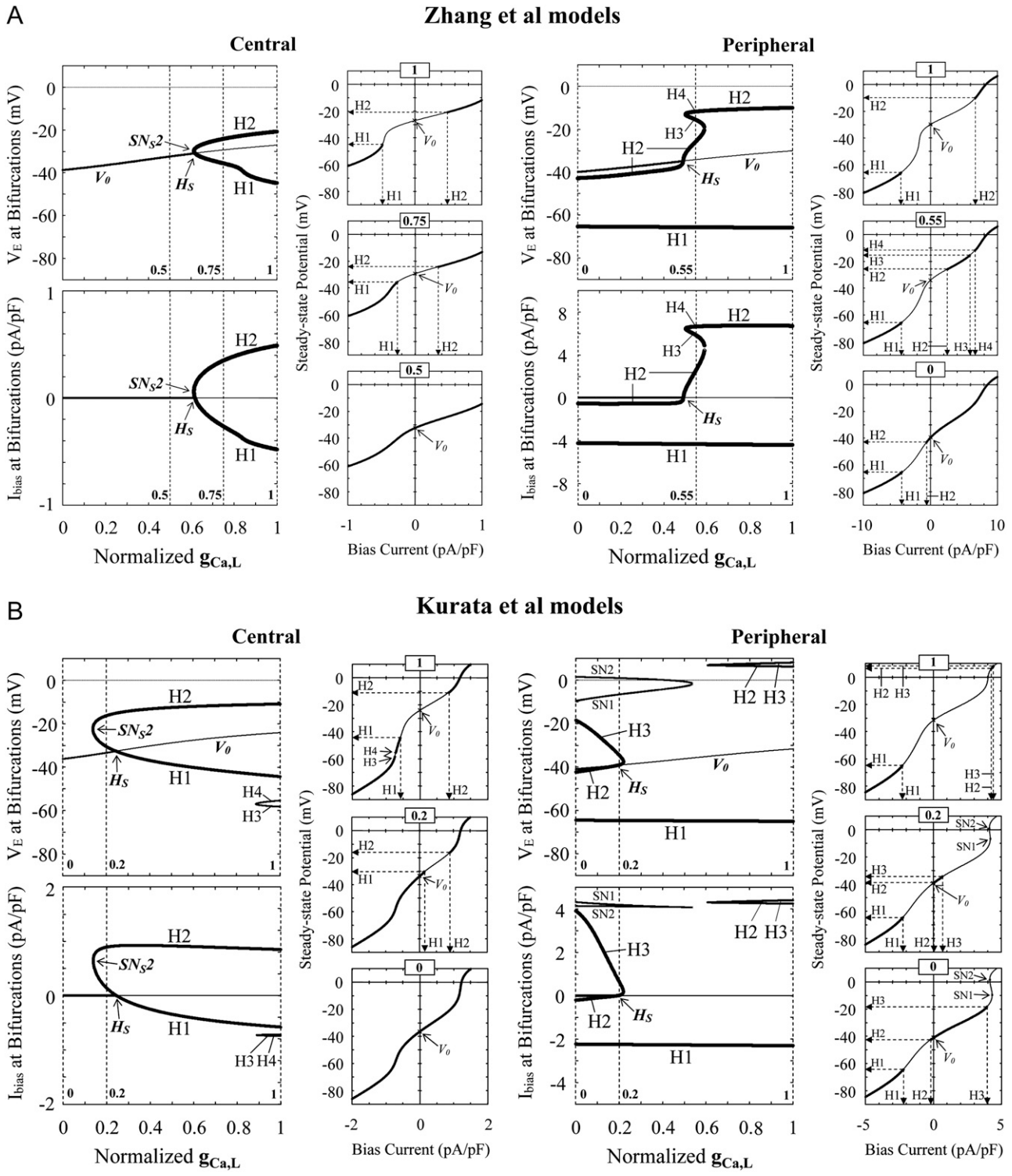

FIGURE 6 Effects of reducing $g_{Ca,L}$ on bifurcation structures (stability and bifurcation of EPs) during I_{bias} applications of the Zhang et al. (*A*) and Kurata et al. (*B*) models for central and peripheral cells. Displacements of Hopf (*H1–H4*) and saddle-node (*SN1*, *SN2*) bifurcation points in the I_{bias}-V_E curve with decreasing $g_{Ca,L}$ at an interval of 0.001 are shown on the potential (V_E) coordinates (*top*) and current (I_{bias}) coordinates (*bottom*). The path of the control V_E at $I_{bias} = 0$ is also shown on the potential coordinates (V_0), intersecting the locus of H1 or H2 at the Hopf bifurcation points (H_S) as shown in Fig. 2. In the insets, V_E and its stability, as well as bifurcation points, are shown as functions of I_{bias} for $g_{Ca,L} = 1$, 0.75, and 0.5 (*A*, *central*); $g_{Ca,L} = 1$, 0.55, and 0 (*A*, *peripheral*); or $g_{Ca,L} = 1$, 0.2, and 0 (*B*), as indicated by the dashed lines. The unstable regions where spontaneous oscillations occur are as follows: *A*, between H1 and H2 (or H3 and H4 in the periphery); *B* (*central*), between H1 and H2 (or H3 and H4); *B* (*peripheral*), between H1 and H2, or above H3 (or above H1 at $g_{Ca,L} = 0.221$–0.605). A codimension-two saddle-node bifurcation point at which the loci of H1 and H2 merge together, i.e., the unstable region disappears, is labeled SN_S2 (codimension-two saddle-node bifurcation of EPs) at $g_{Ca,L} = 0.6131$ (*A*, *central*) and 0.1382 (*B*, *central*).

Effects of blocking ionic currents on bifurcations during I_{bias} applications

To clarify the contributions of sarcolemmal currents to EP instability during applications of I_{bias}, we examined the effects of blocking I_{Na}, I_h or other time-dependent currents on the unstable V_E and I_{bias} regions in the I_{bias}-V_E curve. Hopf and saddle-node bifurcation points in the I_{bias}-V_E curve were determined with decreasing the maximum current conductance and plotted on the potential and current coordinates. The results after the I_{Na} and I_h blocks in the $I_{Ca,L}$-removed systems are shown in Fig. 10. The manner in which blocking each current shrinks the unstable V_E range where spontaneous oscillations occur should be noted; the more prominent the shrinkage in the unstable V_E region, the greater is the contribution of the current to EP instability.

The unstable V_E regions at negative potentials (between H1 and H2) shrunk with decreasing g_{Na} but not with decreasing g_h. In the $I_{Ca,L}$-removed systems, the unstable regions disappeared via a codimension-two saddle-node bifurcation; in contrast, reducing g_h did not shrink the unstable V_E range, not causing a saddle-node bifurcation. Decreases in either g_{Na} or g_h shrunk the unstable current region for hyperpolarizing I_{bias}. The effects of blocking other time-dependent currents were relatively small (data not shown).

Effects of blocking ionic currents on bifurcations during hyperpolarization

For further clarifying how sarcolemmal currents contribute to the relatively high structural stability of the peripheral cells to hyperpolarizing loads, we also examined the effects of blocking individual currents on bifurcation structures of the peripheral cells during ACh applications or electrotonic modulations. Figs. 8 and 9 indicate that a Hopf bifurcation point in the steady-state branch is just or close to the point at which spontaneous activity is abolished by hyperpolarizing loads. To assess the contribution of each current to the structural stability of the peripheral cells, we therefore focused on the changes in Hopf bifurcation points (unstable EP regions). In Figs. 11 and 12, the critical [ACh] or G_C values at which Hopf bifurcations occur are shown as functions of the maximum current conductance.

The critical [ACh] and G_C values most dramatically reduced with decreasing g_{Na}; decreases in g_h or $g_{Ca,L}$ also reduced the critical [ACh] and G_C, but their effects were relatively small. Thus, the robustness against hyperpolarizing loads was most dramatically attenuated by inhibiting I_{Na}. At lower $g_{Ca,L}$ values, two Hopf bifurcation points (H1 and H2) appeared, with the unstable regions where LCs emerge lying between H1 and H2. It should be noted that the unstable regions did not disappear even when $I_{Ca,L}$ was completely blocked. With decreases in g_{Na}, the unstable regions of the $I_{Ca,L}$-removed systems shrunk and finally vanished via codimension-two saddle-node bifurcations; in contrast, they were not significantly or only slightly shrunk by reductions of g_h or $g_{Ca,T}$ (data not shown).

Bifurcation structures of I_{Na}- or I_h-removed peripheral cells

We compared the bifurcation structures during the $I_{Ca,L}$ block of the normal, I_{Na}-removed, and I_h-removed peripheral cells (data not shown). In all the model cells, blocking $I_{Ca,L}$ caused EP stabilization via a Hopf bifurcation. LCs of the I_{Na}-removed systems became unstable via a period-doubling bifurcation with emergence of irregular dynamics, which vanished at the Hopf bifurcation point. The critical $g_{Ca,L}$ values for the bifurcations were higher in the I_{Na}-removed systems than in the control systems. The I_h-removed cells exhibited nearly the same stability, dynamics, and bifurcations during $g_{Ca,L}$ decreases as the normal cells.

Figs. 13 and 14 show the bifurcation structures of the I_{Na}-removed cells as well as of the normal cells during increases of [ACh] and G_C, respectively. In the I_{Na}-removed systems, EPs were stabilized via Hopf bifurcations at smaller [ACh] and G_C values than in the control systems. Stable LCs of the I_{Na}-removed cells became unstable via period-doubling bifurcations, with irregular dynamics emerging between the period-doubling and Hopf bifurcations. The bifurcation values for irregular dynamics and quiescence were far smaller in the I_{Na}-removed systems than in the control systems. The critical [ACh] or G_C value for bifurcations of the I_h-removed cells was also smaller than that of the normal cells but much larger than that of the I_{Na}-removed cells (data not shown; see Figs. 11 and 12).

Searching for I_{Na}-dependent pacemaking in peripheral cells

The $I_{Ca,L}$-removed peripheral cell has an unstable EP region during hyperpolarization (Figs. 4 and 5), which disappears by blocking I_{Na} (Fig. 10). As shown in Fig. 5 *B*, the application of hyperpolarizing I_{bias} to the $I_{Ca,L}$-eliminated peripheral cells yielded destabilization of an EP via a Hopf bifurcation, at which the cells resumed spontaneous activity. Increasing [ACh] or G_C also induced EP destabilization and emergence of a stable LC in the $I_{Ca,L}$-removed peripheral systems (data not shown). Under hyperpolarized conditions, therefore, I_{Na} may be responsible for EP instability and may possibly yield spontaneous oscillations independent of $I_{Ca,L}$. These findings further suggest that the ''I_{Na}-dependent pacemaking'' occurs in hyperpolarized peripheral cells. We assumed that pacemaker activity is I_{Na}-dependent when I_{Na} (not $I_{Ca,L}$) is responsible for the instability of an EP and, thus, an I_{Na} block (but not an $I_{Ca,L}$ block) causes EP stabilization and cessation of spontaneous activity. To determine whether and how the I_{Na}-dependent pacemaking is possible, we further explored bifurcation structures of the hyperpolarized peripheral cells during the I_{Na} and/or $I_{Ca,L}$ blocks.

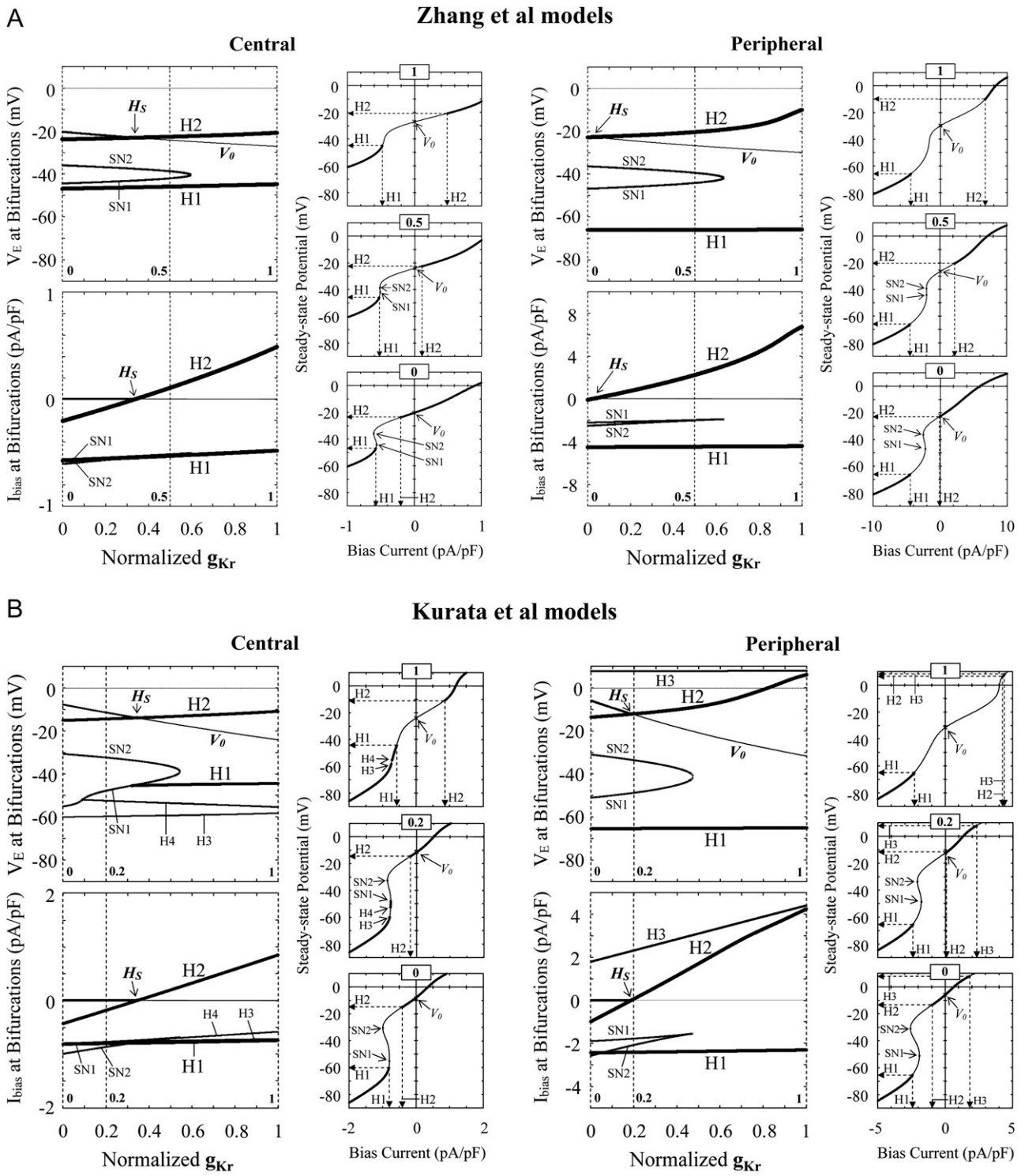

FIGURE 7 Effects of reducing g_{Kr} on bifurcation structures during I_{bias} applications of the Zhang et al. (*A*) and Kurata et al. (*B*) models. Displacements of Hopf (*H1–H4*) and saddle-node (*SN1*, *SN2*) bifurcation points in the I_{bias}-V_E curve with decreasing g_{Kr} at an interval of 0.001 are shown on the potential (*top*) and current (*bottom*) coordinates. The path of V_0 is also shown on the potential coordinates, intersecting the locus of H1 or H2 at the Hopf bifurcation points (H_S) as shown in Fig. 3. In the insets, V_E and its stability, as well as bifurcation points, are shown as functions of I_{bias} for $g_{Kr} = 1$, 0.5, and 0 (*A*) or $g_{Kr} = 1$, 0.2, and 0 (*B*), as indicated by the dashed lines. The unstable regions are as follows: *A*, between H1 and H2; *B* (*central*), between H1 and H2 (or SN1 and H2 at $g_{Kr} < 0.318$), and H3 and H4 (or H3 and SN1 at $g_{Kr} < 0.090$); *B* (*peripheral*), between H1 and H2, and above H3.

Influences of hyperpolarization on bifurcations during inhibition of $I_{Ca,L}$ and/or I_{Na}

We constructed two-parameter bifurcation diagrams in which the loci of Hopf bifurcation of EPs are plotted as functions of $g_{Ca,L}$ and g_{Na} (Fig. 15). ACh was applied to the peripheral cells at various concentrations. The critical $g_{Ca,L}$ value at which a Hopf bifurcation occurs was determined by the stability analysis with g_{Na} fixed at various different values, and was plotted as a function of g_{Na} (for more details, see Appendix C). Note that the right-top corner of the diagrams corresponds to the control condition. In the absence of ACh, an EP was stabilized by reducing $g_{Ca,L}$ but not by reducing g_{Na} (with normal $g_{Ca,L}$). However, increasing [ACh] shifted the loci of Hopf bifurcation points, i.e., changed the stable and unstable regions, in the g_{Na}-$g_{Ca,L}$ plane. With ACh at higher concentrations (Fig. 15, *f–h*), an EP was stabilized by decreasing g_{Na} but not by decreasing $g_{Ca,L}$ (with normal g_{Na}).

Bifurcation structures of hyperpolarized peripheral cells during inhibition of $I_{Ca,L}$ or I_{Na}

Fig. 16 shows the stability, dynamics, and bifurcations of the peripheral cells during $I_{Ca,L}$ or I_{Na} block in the absence and presence of ACh at $1 \times 10^{-6.8}$ M (158.5 nM) for the Zhang et al. model and $1 \times 10^{-7.0}$ M (100 nM) for the Kurata et al. model. Under normal conditions at [ACh] = 0, reducing $I_{Ca,L}$ stabilized an EP and abolished LCs, whereas reducing I_{Na} did not. Under the hyperpolarized conditions, however, blocking I_{Na} caused 1), LC destabilization to induce irregular dynamics via a period-doubling or Neimark-Sacker bifurcation, and 2), EP stabilization via a Hopf bifurcation below which quiescence occurred. In contrast, the abolition (or destabilization) of the stable LC or EP stabilization did not occur during the inhibition of $I_{Ca,L}$ in the hyperpolarized cells.

DISCUSSION

Regional differences in pacemaker mechanism and structural stability

Mechanisms of normal pacemaking are essentially the same for center and periphery

It has been reported that $I_{Ca,L}$ is responsible for EP instability and spontaneous oscillations of the primary pacemaker cell in the rabbit SA node, i.e., natural pacemaking is $I_{Ca,L}$-dependent (2). In the center of the SA node, $I_{Ca,L}$ would contribute to EP destabilization as a prerequisite for robust pacemaking, whereas other time-dependent currents are not necessary for basal pacemaking, rather playing pivotal roles in regulations of pacemaker activity. In this study, pacemaker activities of the peripheral cell models were abolished by blocking $I_{Ca,L}$ but not by blocking I_{Na} or I_h, as in the central cell models (Fig. 1). Bifurcation structures during the $I_{Ca,L}$ block of the

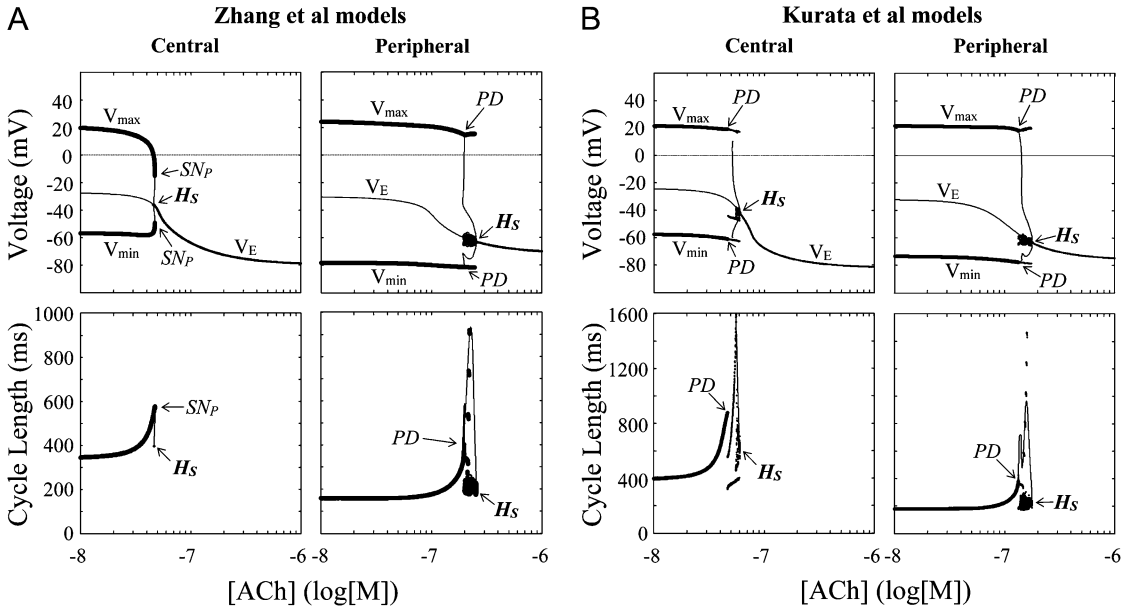

FIGURE 8 Effects of ACh applications (increases in [ACh]) on the stability and dynamics of the Zhang et al. (*A*) and Kurata et al. (*B*) models. One-parameter bifurcation diagrams for [ACh] (log[M]) depicting a locus of V_E and the potential extrema of LCs (V_{min}, V_{max}) are shown (*top*); the CL of LCs is also shown as functions of log[ACh] (*bottom*). For calculations of EPs and stable LCs, the log[ACh] values were increased at the interval of 0.001. Hopf bifurcation points on the steady-state branches are labeled H_S: *A*, at log[ACh] = −7.3332 (*central*) and −6.6059 (*peripheral*); *B*, at log[ACh] = −7.2218 (*central*) and −6.7545 (*peripheral*). The points at which a saddle-node (SN_P) or period-doubling (*PD*) bifurcation of LCs occurs with disappearance of stable LCs are located on the periodic branches: *A*, SN_P at log[ACh] = −7.3239 (*central*); *PD* at log[ACh] = −6.7148 (*peripheral*); *B*, *PD* at log[ACh] = −7.329 (*central*) and −6.874 (*peripheral*). Potential extrema and CLs of the irregular dynamics emerging between *PD* and H_S are also superimposed.

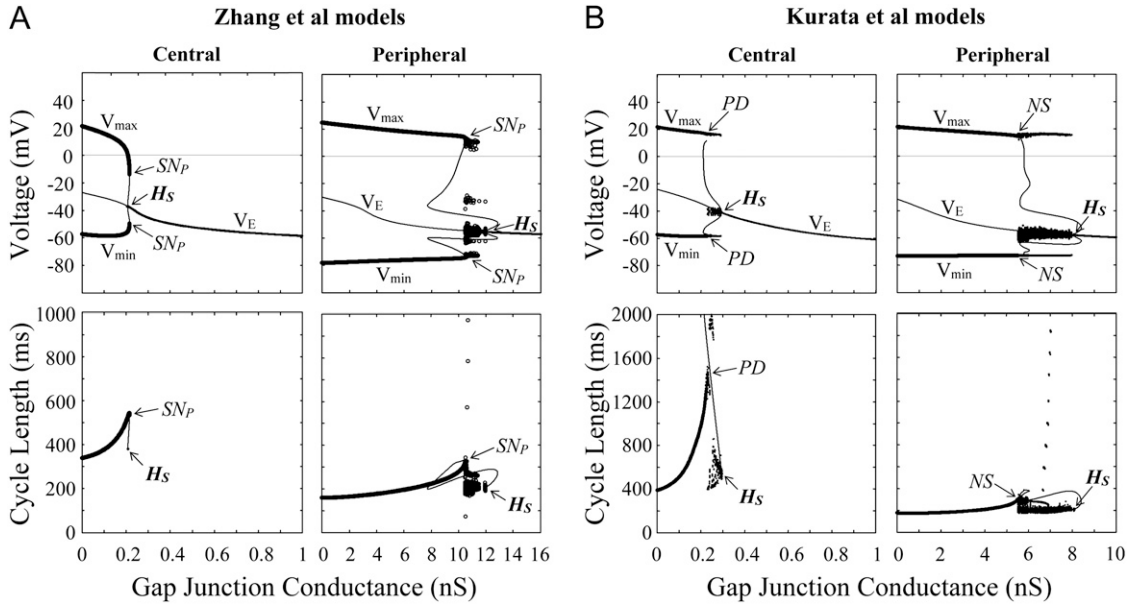

FIGURE 9 Effects of electrotonic loads of the atrium (increases in G_C) on the stability and dynamics of the Zhang et al. (*A*) and Kurata et al. (*B*) models. One-parameter bifurcation diagrams for G_C (nS) depicting a locus of V_E and the potential extrema of LCs (V_{min}, V_{max}) are shown (*top*); the CL of LCs is also shown as functions of G_C (*bottom*). G_C values for the central and peripheral cells were increased at the interval of 0.001 and 0.01 (nS), respectively. Hopf bifurcation points are labeled H_S: *A*, at $G_C = 0.2067$ (*central*) and 11.953 (peripheral); *B*, at $G_C = 0.2925$ (*central*) and 8.0688 (*peripheral*). The points at which a saddle-node (SN_P), period-doubling (*PD*), or Neimark-Sacker (*NS*) bifurcation of LCs occurs are located: *A*, SN_P at $G_C = 0.2152$ (*central*) and 10.484 (*peripheral*); *B*, *PD* at $G_C = 0.230$ (*central*); *NS* at $G_C = 5.51$ (*peripheral*). Potential extrema and CLs of the irregular dynamics emerging between the bifurcation of LCs and H_S are also superimposed.

central and peripheral cells were the same in that an EP was stabilized via a Hopf bifurcation, although the ways of abolishing automaticity were model-dependent (Fig. 2). These findings suggest that the dynamical mechanism of peripheral cell pacemaking is essentially the same as that of central cell pacemaking (2) and that basal pacemaking of the peripheral cell, as well as the central cell, is $I_{Ca,L}$-dependent.

Inconsistent with our simulated results, however, Kodama et al. (3) reported that applications of 2 μM nifedipine causing ~99% block of $I_{Ca,L}$ abolished spontaneous activity in the central region but not in the peripheral region, suggesting an $I_{Ca,L}$-independent pacemaker mechanism for the peripheral SA node. This inconsistency may reflect the relatively small $g_{Ca,L}$ value for bifurcation to quiescence in the peripheral cell (Fig. 2), as well as the incomplete block of $I_{Ca,L}$ or modulations of other currents by the agent in their preparations. Under hyperpolarized conditions, peripheral cell pacemaking was abolished not by blocking $I_{Ca,L}$ but by blocking I_{Na}, i.e., I_{Na}-dependent (Fig. 16). Furthermore, eliminating $I_{Ca,L}$ did not cause either stabilization of an EP (Hopf bifurcation) or cessation of pacemaker activity when relatively high $[Na^+]_i$ was assumed (data not shown). Thus, it is also possible that peripheral cell pacemaking was not $I_{Ca,L}$-dependent in their preparations due to hyperpolarization (outward shift in the net background current) or other unknown reasons. Previous reports also suggest that I_h plays a predominant role in the subsidiary pacemaker mechanisms (4–6). I_{Na} or I_h might contribute to EP destabilization and pacemaker generation in hyperpolarized peripheral SA node cells.

Structural stability to hyperpolarization of peripheral cell is greater than that of central cell

Our results suggest that the peripheral cell is considerably more robust than the central cell against hyperpolarizing loads such as applications of ACh (or hyperpolarizing I_{bias}) and electrotonic modulations by atrial myocytes (Figs. 6–9). Zhang et al. (30) also reported the lower sensitivity of the peripheral cell model to ACh. It should be noted that the structural stability of the peripheral cell against electrotonic loads was much greater than that of the central cell (Fig. 9). The higher structural stability of the peripheral cell is reasonable because in vivo peripheral cells are directly exposed to electrotonic loads of adjacent atrial myocytes, and thus must be more robust against hyperpolarizing loads than central cells.

The higher structural stability to hyperpolarization of the peripheral cell may be related to the pacemaker shift from the center to the periphery in SA node tissues under hyperpolarized conditions (36,37). Although it is not known whether there is a regional difference in the density of muscarinic K^+ channels, that of muscarinic M_2 receptors as well as vagal innervation was reported to be greater in the center than in the periphery (31,32). As Shibata et al. (37) suggested, the pacemaker shift may be the result of the regional differences in the robustness against hyperpolarizing loads,

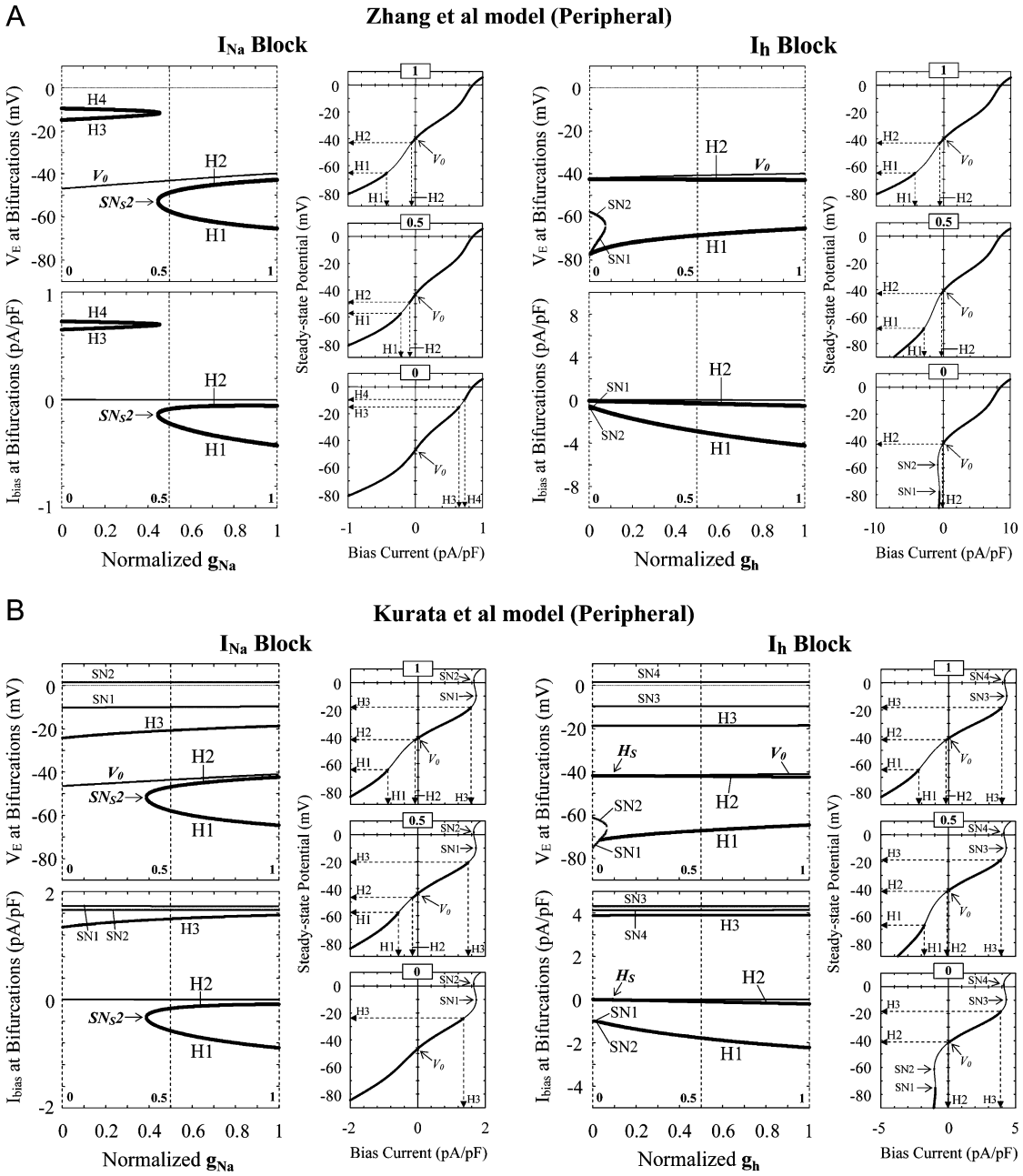

FIGURE 10 Effects of blocking I_{Na} or I_h on bifurcation structures during I_{bias} applications of the $I_{Ca,L}$-removed Zhang et al. (*A*) and Kurata et al. (*B*) peripheral models. Displacements of Hopf (*H1–H4*) and saddle-node (*SN1–SN4*) bifurcation points in the I_{bias}-V_E curve with decreasing g_{Na} or g_h at an interval of 0.001 are shown on the potential (*top*) and current (*bottom*) coordinates. The path of V_0 is also shown on the potential coordinates. In the insets, V_E and its stability, as well as bifurcation points, are shown as functions of I_{bias} for $g_{Ca,L} = 1$, 0.5, and 0, as indicated by the dashed lines. The unstable regions where spontaneous oscillations occur are as follows: *A*, between H1 and H2 (or H3 and H4); *B*, between H1 (or SN1) and H2, or above H3. A codimension-two saddle-node bifurcation point at which the loci of H1 and H2 merge together is labeled SN_S2 at $g_{Na} = 0.4470$ (*A*) and 0.388 (*B*).

M_2 receptor density, vagal innervation, and possibly $I_{K,ACh}$ density as well.

Contribution of intracellular Ca^{2+} dynamics to regional differences

Lancaster et al. (38) reported that the effect of 2–30 μM ryanodine on CL was greater in peripheral cells (24 ± 6% increase) than in central cells (3.5 ± 2% increase). This may be related to heterogeneous expression of Ca^{2+} handling proteins (39), which might contribute to the regional differences in dynamical properties of pacemaker activities. Inconsistent with their experimental findings, our peripheral model could exhibit only a small increase in CL (10.7–14.0%) on minimizing the SR Ca^{2+} release, whereas a central version with a larger response (~112.2% increase in CL) could be devel-

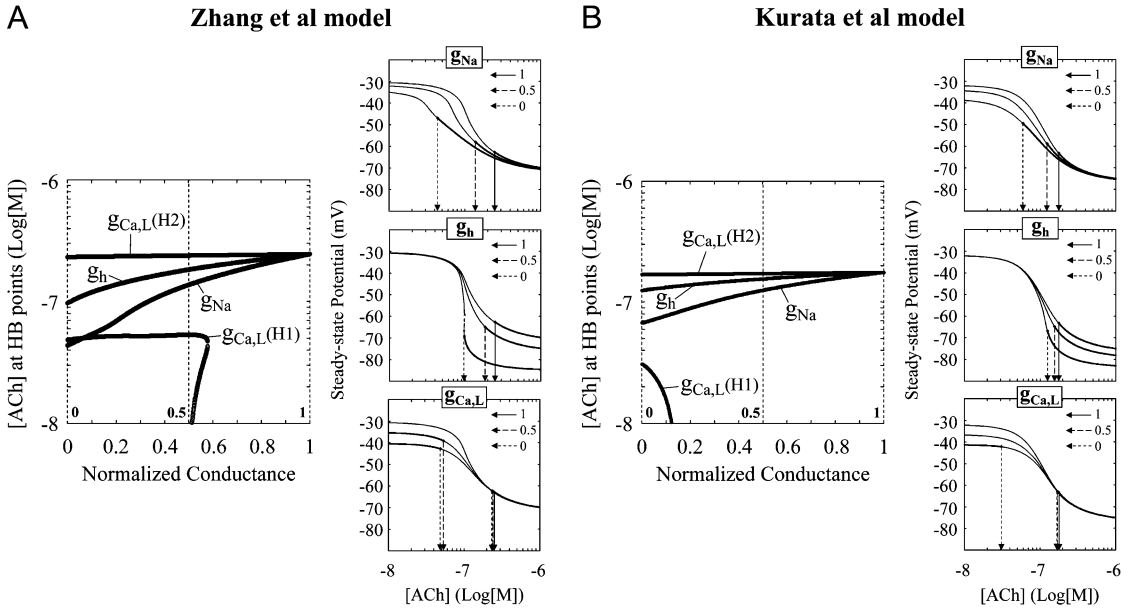

FIGURE 11 Effects of blocking individual currents on bifurcations during ACh applications of the Zhang et al. (*A*) and Kurata et al. (*B*) peripheral models. Two-parameter bifurcation diagrams for the normalized maximum current conductance (abscissa) and log[ACh] (ordinate) are shown; the critical [ACh] values at Hopf bifurcation points were plotted as functions of the conductance, which was decreased at an interval of 0.001. The values of [ACh] (log[M]) were increased at an interval of 0.001 for searching for bifurcation points. In the insets, one-parameter bifurcation diagrams for log[ACh] used for construction of the two-parameter diagrams are shown for g_{Na}, g_h, and $g_{Ca,L}$ at 1, 0.5, and 0, as indicated by the dashed lines in the two-parameter diagrams.

oped. The relatively small response of the peripheral model appeared to be due to the presence of large I_{Na} because the model cell with reduced I_{Na} exhibited much greater response, e.g., 34.3–39.6% increases in CL with $g_{Na} = 0.3$ (data not shown). In addition, ryanodine or BAPTA are known to affect sarcolemmal ion channel currents probably via decreasing intracellular Ca^{2+} concentrations (40); their secondary (or direct) effects on ionic channels may result in more dramatic responses of peripheral cells with higher densities of the channels.

To clarify whether SR Ca^{2+} cycling and intracellular Ca^{2+} dynamics substantially alter the dynamical properties of SA node cells and contribute to the regional differences in bifurcation structures, we explored their influences on stability and bifurcation of the Kurata et al. models (see Theory and Methods). Changes in SR Ca^{2+} uptake and release rates only slightly affected the stability and bifurcation of the model cells; bifurcation structures of the modified models with larger responses to the suppression of SR Ca^{2+} release were essentially the same as those of the original systems with smaller responses (data not shown). We therefore believe that neither SR Ca^{2+} cycling nor intracellular Ca^{2+} dynamics exerts substantial effects on the dynamical properties of SA node cells, not significantly contributing to the regional differences in bifurcation structures. This idea is also supported by the fact that the bifurcation structures of the Kurata et al. models incorporating the intracellular Ca^{2+} dynamics were essentially the same as those of the Zhang et al. models with fixed $[Ca^{2+}]_i$.

Roles of I_{Na} in peripheral cell pacemaking

I_{Na} contributes to high structural stability of peripheral cell

The I_{Na} block most dramatically shrunk the [ACh] and G_C regions, as well as the I_{bias} region, of unstable EP where LCs emerge (Figs. 10–12), suggesting that I_{Na} mainly contributes to the relatively high structural stability of peripheral cells. This idea was further supported by the finding that the I_{Na}-incorporated system exhibited robust pacemaking over the broader ranges of [ACh] and G_C than the I_{Na}-removed system; spontaneous oscillations of the I_{Na}-removed system were unstable in frequency and ceased at relatively low [ACh] or G_C values (Figs. 13 and 14). Consistent with our result, Watanabe et al. (33) reported that an SA node cell with a relatively small maximum upstroke velocity (i.e., including only small I_{Na}) had a relatively low threshold G_C (0.58 nS) in causing bifurcation to quiescence or irregular dynamics. Thus, I_{Na} may dramatically improve the structural stability of peripheral cells, playing a pivotal role in preventing a bifurcation to quiescence or irregular dynamics, as well as an excess increase in CL, during hyperpolarization.

I_{Na} in peripheral cells is also suggested to help the SA node in driving the atrium, i.e., it plays an important role in the conduction of pacemaker activity to atrial myocytes. Reduction of I_{Na} in the peripheral SA node slows down the pacemaking rate (not only in the periphery but also in the center), decreases the conduction velocity, and causes exit block or sinus arrest (41,42). Thus, SA node dysfunctions in

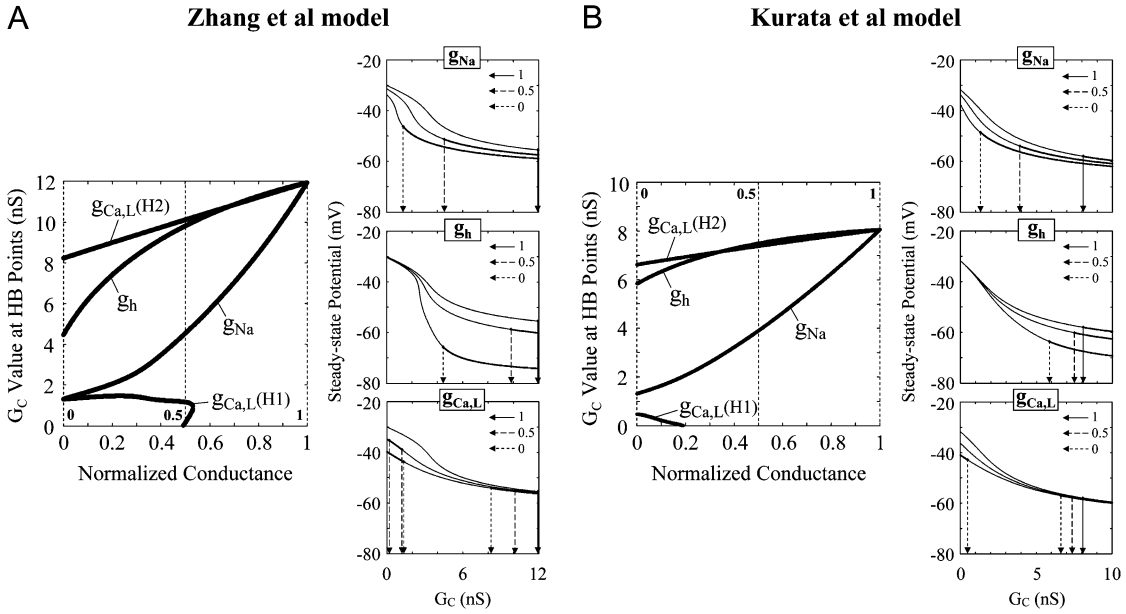

FIGURE 12 Effects of blocking individual currents on bifurcations during electrotonic modulations of the Zhang et al. (*A*) and Kurata et al. (*B*) peripheral models. Two-parameter bifurcation diagrams for the normalized maximum current conductance (abscissa) and G_C (ordinate) are shown; the critical G_C values at Hopf bifurcation points were plotted as functions of the conductance, which was decreased at an interval of 0.001. The values of G_C (nS) were increased at an interval of 0.01 for searching for bifurcation points. In the insets, one-parameter bifurcation diagrams for G_C used for construction of the two-parameter diagrams are shown for g_{Na}, g_h, and $g_{Ca,L}$ at 1, 0.5, and 0, as indicated by the dashed lines in the two-parameter diagrams.

congenital sick sinus syndromes and aged hearts may be at least in part due to the I_{Na} decrease in peripheral cells (43,44). Our results and these reports suggest that I_{Na} is indispensable for the robust maintenance of SA node pacemaking and driving against electrotonic loads of the atrium.

Possible I_{Na}-dependent pacemaking in hyperpolarized peripheral cell

The $I_{Ca,L}$-removed peripheral cell resumed spontaneous activity when an EP was destabilized via a Hopf bifurcation by hyperpolarizing loads (Fig. 5). In the $I_{Ca,L}$-removed periph-

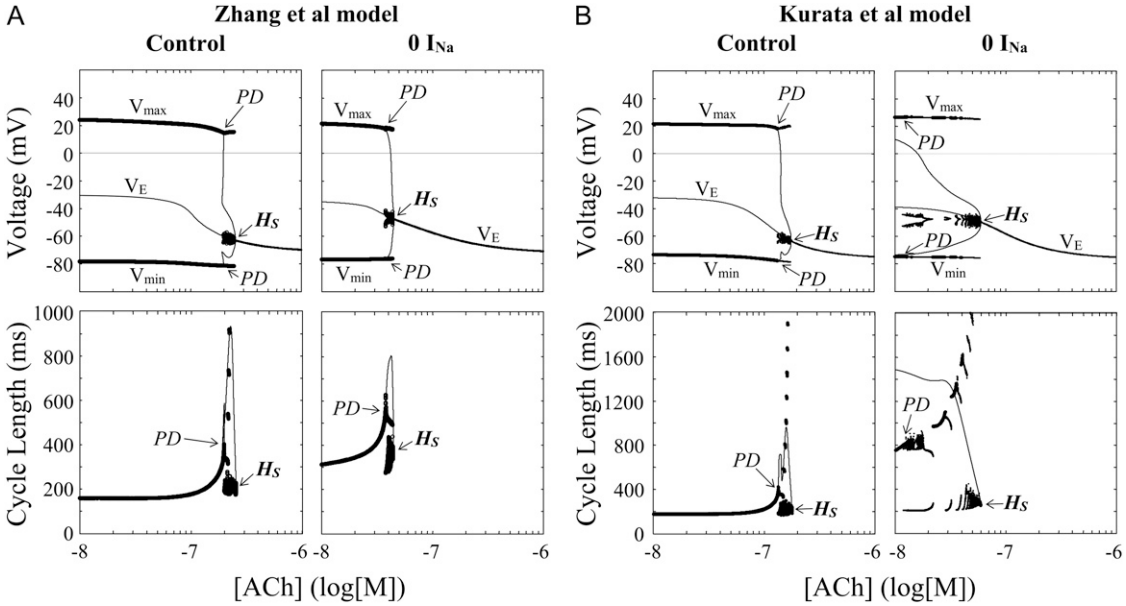

FIGURE 13 Bifurcation structures during ACh applications of the normal (*control*) and I_{Na}-removed (0 I_{Na}) versions of the Zhang et al. (*A*) and Kurata et al. (*B*) peripheral models. One-parameter bifurcation diagrams for log[ACh] depicting the steady-state (V_E) and periodic (V_{min}, V_{max}) branches are shown (*top*); the CL of LCs is also shown as functions of log[ACh] (*bottom*). Procedures of the calculations are the same as for Fig. 8. Hopf (H_S) and period-doubling (*PD*) bifurcation points are located: *A*, H_S at log[ACh] = −6.6059 (*control*) and −7.3586 (0 I_{Na}); *PD* at log[ACh] = −6.7148 (*control*) and −7.4250 (0 I_{Na}); *B*, H_S at log[ACh] = −6.7545 (*control*) and −7.2241 (0 I_{Na}); *PD* at log[ACh] = −6.874 (*control*) and −7.930 (0 I_{Na}).

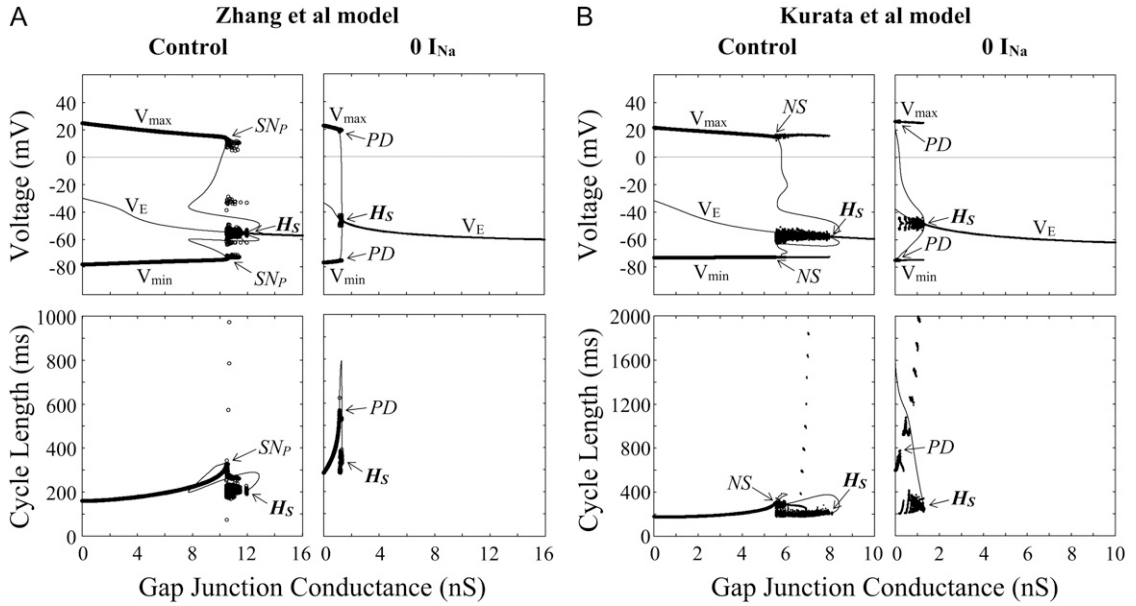

FIGURE 14 Bifurcation structures during electrotonic modulations of the normal (*control*) and I_{Na}-removed (0 I_{Na}) versions of the Zhang et al. (*A*) and Kurata et al. (*B*) peripheral models. One-parameter bifurcation diagrams for G_C depicting the steady-state (V_E) and periodic (V_{min}, V_{max}) branches are shown (*top*); the CL of LCs is also shown as functions of G_C (*bottom*). Procedures of the calculations are the same as for Fig. 9. Hopf (H_S), saddle-node (SN_P), period-doubling (*PD*), and Neimark-Sacker (*NS*) bifurcation points are located: *A*, H_S at $G_C = 11.953$ (*control*) and 1.3152 (0 I_{Na}); SN_P at $G_C = 10.484$ (*control*); *PD* at $G_C = 1.1380$ (0 I_{Na}); *B*, H_S at $G_C = 8.0688$ (*control*) and 1.3170 (0 I_{Na}); *PD* at $G_C = 0.15$ (0 I_{Na}); *NS* at $G_C = 5.51$ (*control*).

eral cell, the unstable I_{bias}, [ACh], or G_C region where stable or unstable LCs appear vanished via a codimension-two saddle-node bifurcation during I_{Na} inhibition, but not during I_h or $I_{Ca,T}$ inhibition (Fig. 10). These results suggest that the spontaneous oscillation of the $I_{Ca,L}$-removed system is I_{Na}-dependent and that I_{Na} destabilizes an EP and induces spontaneous oscillations independent of $I_{Ca,L}$ in hyperpolarized peripheral cells.

Our results further suggest that I_{Na}-dependent pacemaking is possible under hyperpolarized conditions (Figs. 15 and 16). An I_{Na} block by tetrodotoxin abolished pacemaker activity of the peripheral region of the intact SA node that suffers electrotonic loads of the atrium (41,42). Previous studies also suggest the requirement of I_{Na} for murine SA node pacemaking (41,42) and for pacemaking in human embryonic stem cell-derived cardiomyocytes that did not require $I_{Ca,L}$ or I_h (45). Thus, I_{Na}-dependent pacemaking may actually occur in hyperpolarized peripheral SA node cells, as well as in other pacemaker cells.

Significance of applying bifurcation theory to pacemaker system analyses

In this study, we employed stability and bifurcation analyses to investigate the regional difference in the mechanisms and robustness of pacemaker activity, and also the roles of I_{Na} in peripheral cell pacemaking. Our work clearly shows that the nonlinear dynamical approach allows us to identify key variables or parameters responsible for pacemaker generation and to define the contribution of each current to pacemaking. As previous studies have indicated, bifurcation analyses of SA node or ventricular models are necessary for general understanding and systematic descriptions of the dynamical mechanisms of natural pacemaking (2), abnormal automaticity (7–13), and triggered activity (46).

Our study also suggests that exploring bifurcation structures of model cells can reveal the conditions and ways for oscillatory behaviors to emerge or disappear, and possibly allow us to accurately predict and properly control the dynamics and bifurcation structures of real cells. Thus, the mathematical approach based on the bifurcation theory possibly leads to the appropriate design of a structurally stable pacemaker cell system. As suggested previously, it may be applicable to the engineering of biological pacemakers from native cardiomyocytes in vivo (47–49) or human embryonic stem cells ex vivo (17,50,51) for gene or cell therapy of bradyarrhythmias (for review, see (13,17,18)). Our findings regarding the regional differences in bifurcation structures of SA node cells would be useful as a theoretical background for the engineering of biological pacemakers with robust pacemaking and driving similar to the SA node.

Limitations and perspectives of study

Possible disadvantage of using simplified models

Limitations of our study include incompleteness of the models. The model systems used in this study were constructed as base models to reproduce the normal pacemaker activities of central and peripheral cells under basal conditions (14–16). These simplified models could reproduce the experimentally ob-

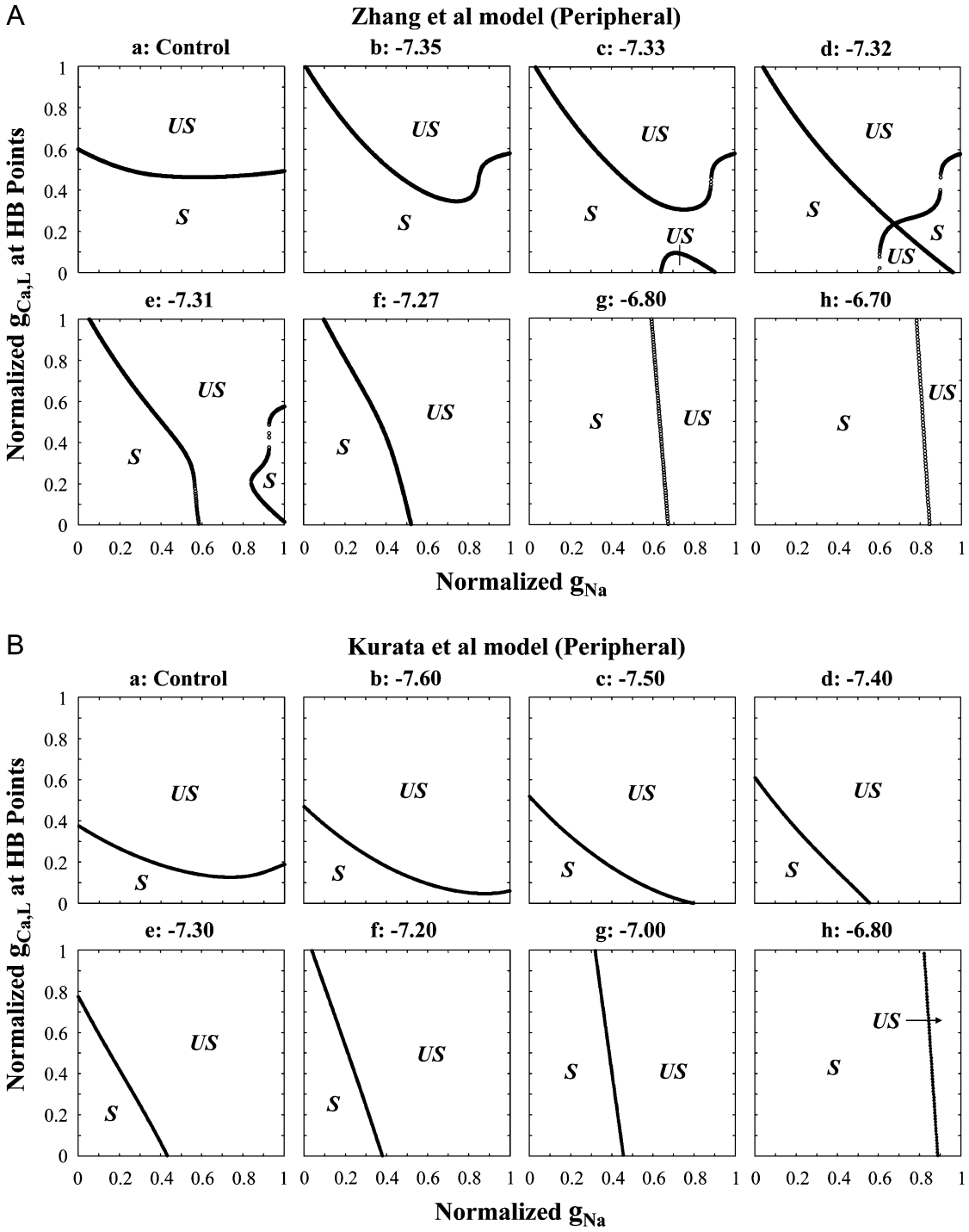

FIGURE 15 EP stability and bifurcation during decreases in $g_{Ca,L}$ and/or g_{Na} of the Zhang et al. (*A*) and Kurata et al. (*B*) peripheral models in the presence of ACh at various concentrations. Each panel shows a two-parameter bifurcation diagram for $g_{Ca,L}$ and g_{Na}, depicting the loci of Hopf bifurcation points. Values of [ACh] are shown at the top of each panel in log[M]. The normalized $g_{Ca,L}$ value was decreased from 1 to 0 at an interval of 0.001 for searching for bifurcations, with g_{Na} fixed at various values; the g_{Na} value was decreased from 1 to 0 at an interval of 0.001 (see Appendix C). Critical $g_{Ca,L}$ values at which Hopf bifurcations occurred were determined and plotted as functions of g_{Na}. The symbols *S* and *US* represent the stable and unstable EP regions, respectively.

served regional differences in dynamic properties of the central and peripheral cell pacemaking (15). However, they do not include detailed descriptions for intracellular Ca^{2+} dynamics, SR Ca^{2+} handling, or activities of other modulating factors. These intracellular factors are known to exert substantial effects on ion channel functions and pacemaker dynamics (e.g., see (52–55)) and possibly affect bifurcation structures as well. Moreover, the regional differences in the activity of Ca^{2+}

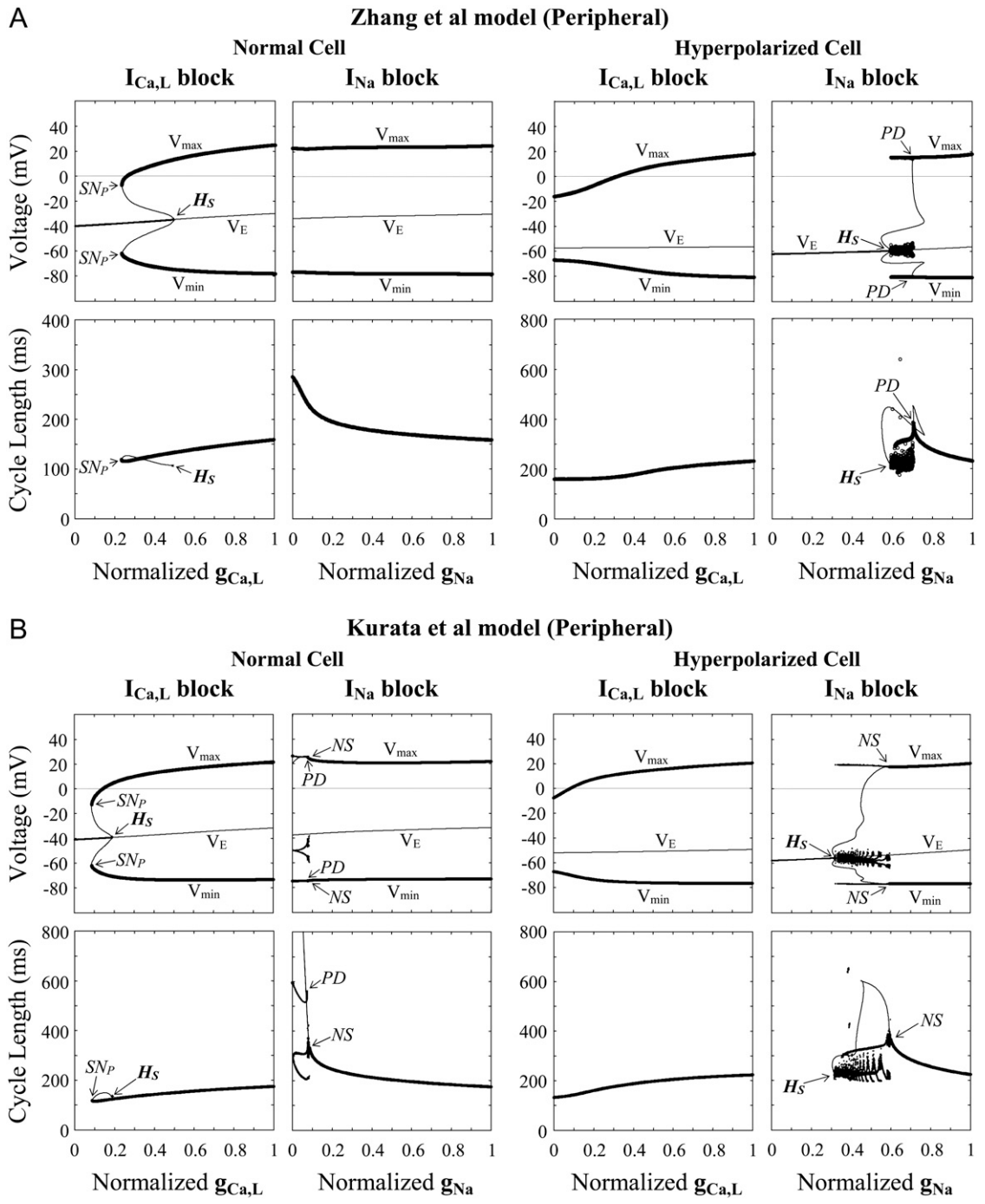

FIGURE 16 Bifurcation structures of the normal and hyperpolarized peripheral cells during the block of $I_{Ca,L}$ or I_{Na}. Both the Zhang et al. (*A*) and Kurata et al. (*B*) models were tested. One-parameter bifurcation diagrams for $g_{Ca,L}$ or g_{Na} depicting steady-state (V_E) and periodic (V_{min}, V_{max}) branches were constructed for the peripheral cells in the absence (*left*) and presence (*right*) of ACh (*top*); the CL of LCs is also shown as functions of $g_{Ca,L}$ or g_{Na} (*bottom*). The [ACh] values for the Zhang et al. and Kurata et al. models are $1 \times 10^{-6.8}$ and $1 \times 10^{-7.0}$ M (158.5 and 100 nM), respectively. Procedures of the calculations are the same as for Fig. 2. Hopf (H_S), saddle-node (SN_P), period-doubling (*PD*), and Neimark-Sacker (*NS*) bifurcations are located: *A*, H_S at $g_{Ca,L} = 0.4912$ (*normal*) and $g_{Na} = 0.5917$ (*hyperpolarized*); SN_P at $g_{Ca,L} = 0.2337$ (*normal*); *PD* at $g_{Na} = 0.7073$ (*hyperpolarized*); *B*, H_S at $g_{Ca,L} = 0.1891$ (*normal*) and $g_{Na} = 0.3178$ (*hyperpolarized*); SN_P at $g_{Ca,L} = 0.085$ (*normal*); *PD* at $g_{Na} = 0.074$ (*normal*); *NS* at $g_{Na} = 0.084$ (*normal*) and 0.595 (*hyperpolarized*).

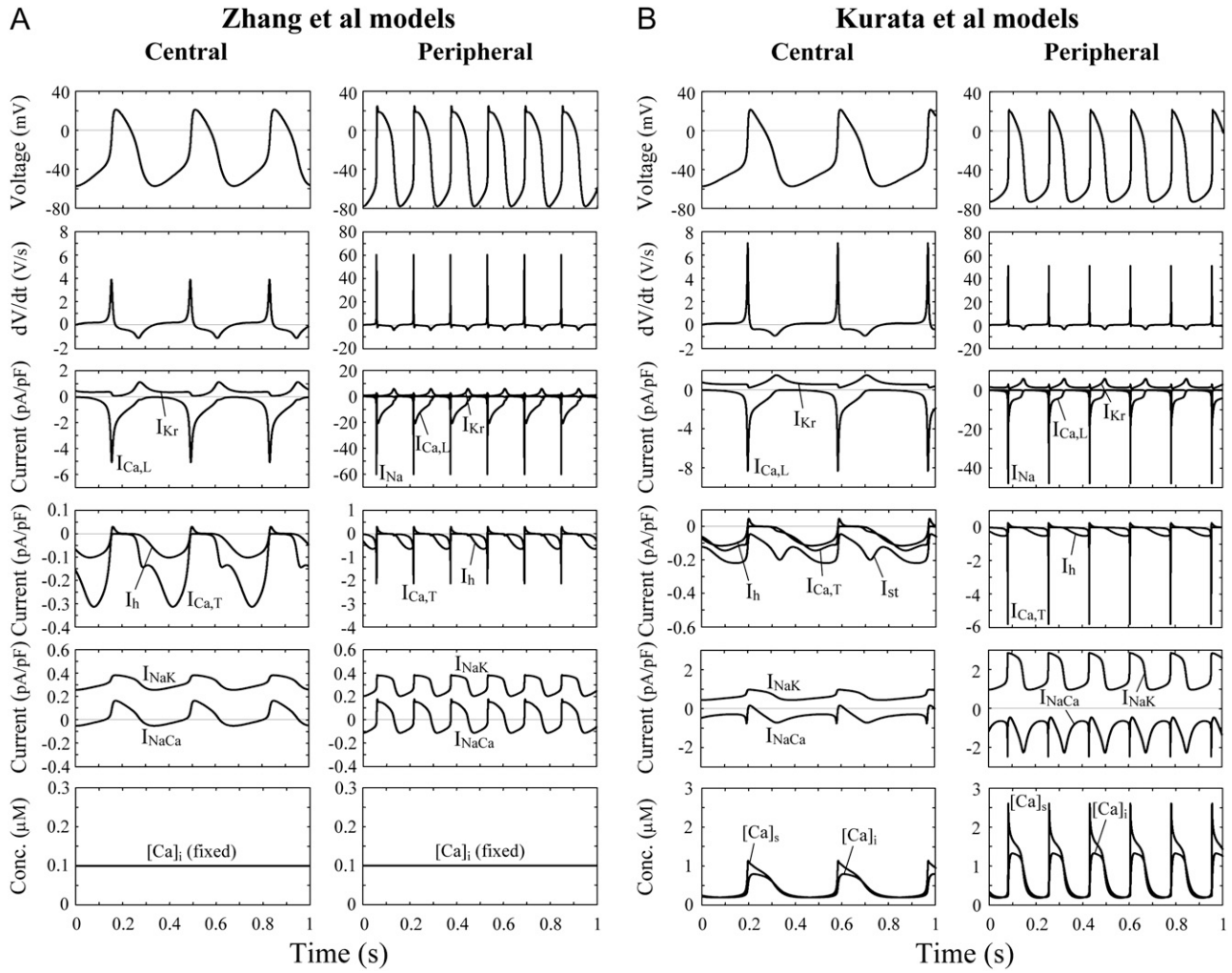

FIGURE 17 Steady-state behaviors of spontaneous APs, underlying transmembrane ionic currents, and intracellular Ca^{2+} dynamics simulated by the central and peripheral versions of the Zhang et al. (*A*) and Kurata et al. (*B*) models with the standard parameter values. Differential equations were numerically solved for 11 s (*A*) or 181 s (*B*) with initial conditions appropriate to an EP and a 1-ms stimulus of 1 pA/pF. Model cell behaviors during the last 1 s starting from maximum diastolic potential are depicted. Intracellular Ca^{2+} dynamics include the changes of Ca^{2+} concentrations in subspace ($[Ca^{2+}]_S$) and myoplasm ($[Ca^{2+}]_i$).

regulatory proteins including the Na^+/Ca^{2+} exchanger, SR Ca^{2+} release channel, and SR Ca^{2+} pump were not taken into account or not based on detailed experimental data; the densities and activities of these proteins are probably greater in the periphery than in the center (38,39).

Another shortcoming of our models may be the use of the classical Hodgkin-Huxley formalism for the kinetic formulation of the time-dependent currents including I_{Na}. More general and realistic schemes, i.e., Markovian state models have been developed for the Na^+ channel (56,57) as well as for other individual channels. However, we did not use these models for I_{Na}, because 1), no Markovian state scheme is available for the SA node Na^+ channel, 2), more detailed experimental data from SA node cells are required for the Markov scheme-based formulation of the SA node I_{Na} kinetics, and 3), such complex models are less suitable for bifurcation analyses. Nevertheless, further sophisticated models based on Markovian state schemes, such as for ventricular myocytes (58), need to be developed and tested for SA node cells in future investigations.

Influences of lacking Ca^{2+} clock

The most serious drawback of the models may be the lack of a ''Ca^{2+} clock'' that is defined as the spontaneous rhythmic Ca^{2+} release from the junctional SR. Blocking the Ca^{2+} clock by ryanodine or BAPTA dramatically increased CL and finally abolished pacemaker activity (59–63); thus, the Ca^{2+} clock may exert substantial effects on the dynamical properties of SA node cells. Nevertheless, we assumed that the basal pacemaking of SA node cells is attributable to the interplay of sarcolemmal ionic currents such as $I_{Ca,L}$, I_{Na}, I_h, and I_{Kr} (i.e., ''membrane clock''), for the following reasons:

1. Experimental reports on the effects of eliminating SR Ca^{2+} release or intracellular Ca^{2+} transient were controversial. In other experimental studies, ryanodine or BAPTA did not abolish, but only slowed, SA node pacemaking (38,

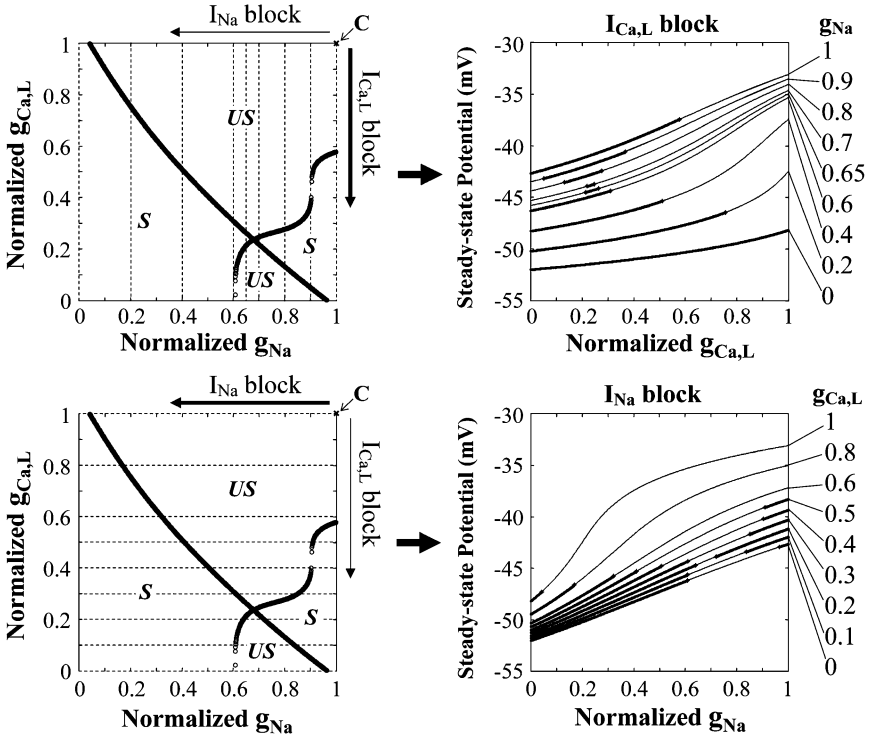

FIGURE 18 How to construct the two-parameter bifurcation diagram for $g_{Ca,L}$ and g_{Na} (Fig. 15) from one-parameter bifurcation diagrams for $g_{Ca,L}$ or g_{Na}. (*Left*) The two-parameter bifurcation diagram for the Zhang et al. peripheral model with the [ACh] of $1 \times 10^{-7.32}$ M (47.863 nM). The point labeled *C* corresponds to the control condition. The leftward and downward shifts from *C* indicate the block of I_{Na} and $I_{Ca,L}$, respectively (shown by the *arrows*). Dashed lines designate the points of g_{Na} (*top*) or $g_{Ca,L}$ (*bottom*) for the construction of the one-parameter bifurcation diagrams shown on the right. (*Right*) One-parameter bifurcation diagrams depicting V_E and its stability as functions of $g_{Ca,L}$ (*top*) or g_{Na} (*bottom*). The normalized $g_{Ca,L}$ (*top*) or g_{Na} (*bottom*) value as the first parameter was decreased from 1 to 0 at an interval of 0.001 for searching for Hopf bifurcations, with the second parameter g_{Na} (*top*) or $g_{Ca,L}$ (*bottom*) fixed at various values as shown on the right of each panel. Critical values of the first parameter $g_{Ca,L}$ (*top*) or g_{Na} (*bottom*) at which Hopf bifurcations occurred were determined by the stability analysis. The thick and thin segments are the stable and unstable V_E regions, respectively; the boundaries between the two segments correspond to the bifurcation points. The two-parameter bifurcation diagram can be constructed by plotting these bifurcation values of the first parameter $g_{Ca,L}$ (or g_{Na}) as functions of the second parameter g_{Na} (or $g_{Ca,L}$).

64,65); thus, the Ca^{2+} clock is not necessarily required for pacemaker generation.

2. Ryanodine and BAPTA are known to affect not only the Ca^{2+} clock but also the membrane clock (40); their secondary (or direct) effects on the membrane clock, rather than the elimination of the Ca^{2+} clock, may result in the dramatic responses.

3. Spontaneous Ca^{2+} release was local (not global), stochastic, and transient in the pacemaker potential range (60); thus, the manner in which the Ca^{2+} clock contributes to the stability and bifurcation structures of SA node cells is unclear. In our opinion, the Ca^{2+} clock is not a prerequisite for basal SA node pacemaking, although it would significantly modulate pacemaker activity and is possibly involved in the regional differences in pacemaker dynamics (38).

As already mentioned, neither SR Ca^{2+} cycling nor intracellular Ca^{2+} dynamics exerted substantial effects on the stability and bifurcation of SA node model cells, with their effects being too small to alter our conclusions. The simplified models used in this study are therefore valuable and highly appropriate for exploring the bifurcation structures of pacemaker cells and essential mechanisms of basal SA node pacemaking. Nevertheless, our models do not incorporate the real Ca^{2+} clock defined as the spontaneous rhythmic Ca^{2+} release from the junctional SR to trigger the membrane clock. We could produce a model with the spontaneous SR Ca^{2+} release (and a transient increase in $[Ca^{2+}]_{sub}$ and the forward-mode I_{NaCa}) during phase 4 depolarization by further increasing SR Ca^{2+} uptake and release rates (data not shown). However, such a model was not used because an excess increase of the SR Ca^{2+} uptake and release rates resulted in very small CL (<150 ms in the peripheral model) and often induced irregular dynamics. Maltsev et al. (66) developed a modified version of the Kurata et al. model (14) to exhibit the spontaneous local Ca^{2+} release from the junctional SR during phase 4. However, their formulas were based on phenomenological representation to approximate the experimental pattern of Ca^{2+} signals in the subspace, which were not suitable for bifurcation analysis. More elaborate models incorporating detailed descriptions of the intracellular Ca^{2+} handling as well as other modulating factors need to be developed for future investigations regarding the role of the Ca^{2+} clock in SA node pacemaking in terms of nonlinear dynamics and bifurcation theory.

Requirement of multicellular models

We used the single-cell or coupled-cell systems to investigate the robustness of SA node pacemaking against hyperpolarization and the roles of I_{Na} in peripheral cell pacemaking. However, the real intact SA node has complex architectures to facilitate optimization of the electrical loading by the surrounding atrial tissue (36,67–69). Previous studies suggest that electrotonic interaction is involved in the pacemaker mechanisms of the intact SA node (5,69). Thus, multicellular models including central and peripheral SA node cells and also atrial myocytes are required for further investigating how electrotonic interactions, as well as I_{Na}, contribute to the pacemaking and driving ability of the intact SA node in vivo. Modeling SA node tissues would also be useful in exploring

the mechanisms of pacemaker shifts (36,37), pacemaker synchronization (70), and abnormal rhythms such as the exit block and intranodal reentry (42).

Lack of experimental evidence

The conclusions in this study are, of course, the predictions from the model cell systems; thus they must be verified and supported by experimental works using real SA node cells. Fundamental properties of the model cell behaviors have been verified by Zhang et al. (15). Inconsistent with our result, however, pacemaker activity of the peripheral cell was not abolished by blocking $I_{Ca,L}$ in either their simulation or in experiments (3). We could not find experimental evidence for the cessation of peripheral cell pacemaking by the inhibition of $I_{Ca,L}$ as predicted by the models in Figs. 1 and 2, although the I_{Na} block was observed to abolish pacemaker activity of the peripheral SA node region with electrotonic loads of the atrium in mice (41,42). Whether an $I_{Ca,L}$ blocker can abolish peripheral cell pacemaking should be reexamined in future experiments. To the best of our knowledge, there is no systematic study regarding the bifurcation structures of SA node cells to clarify the regional differences in the dynamical mechanism and the robustness of pacemaker activity. We hope that this study provides a stimulus to further experimentation on these issues.

APPENDIX A: MODEL EQUATIONS

Mathematical expressions, definitions of the symbols, and standard parameter values used in this study are essentially the same as those in the original articles (14–16). The formulas for $I_{Ca,L}$, I_h, and $I_{K,ACh}$ with ACh modifications of Dokos et al. (29), as well as those for I_{Na} adopted from Garny et al. (16), are given below for convenience. Units are mV, pA, nS, ms, pF, mM, and L (pA/pF and nS/pF for ionic currents and conductance, respectively). Dynamics of the model cells with standard parameter values (for the Kurata et al. models; see Table 1) are shown in Fig. 17.

Na^+ channel current (I_{Na}):

$$I_{Na} = g_{Na} \times [Na^+]_o \times F \times (F/RT) \times V \times \{\exp[(V - E_{Na}) \times F/RT] - 1\}/[\exp(V \times F/RT) - 1] \times m^3 \times [(1 - F_{Na}) \times h_1 + F_{Na} \times h_2] \quad (A1)$$

$$m_\infty = \{1 + \exp[-(V + 30.32)/5.46]\}^{-1/3} \quad (A2)$$

$$h_\infty = \{1 + \exp[(V + 66.1)/6.4\}^{-1} \quad (A3)$$

$$\tau_m = 0.6247/\{0.8322166 \times \exp[-0.33566 \times (V + 56.7062)] + 0.6274 \times \exp[0.0823 \times (V + 65.0131)]\} + 0.04569 \quad (A4)$$

$$\tau_{h1} = 0.003717 \times \exp[-0.2815 \times (V + 17.11)]/\{1 + 0.003732 \times \exp[-0.3426 \times (V + 37.76)]\} + 0.5977 \quad (A5)$$

$$\tau_{h2} = 0.00003186 \times \exp[-0.6219 \times (V + 18.8)]/\{1 + 0.00007189 \times \exp[-0.6683 \times (V + 34.07)]\} + 3.556 \quad (A6)$$

$$F_{Na} = 0.09518 \times \exp(-0.06306 \times (V + 34.4))/\{1 + 1.662 \times \exp[-0.2251 \times (V + 63.7)]\} + 0.08693. \quad (A7)$$

L-type Ca^{2+} channel current ($I_{Ca,L}$) for modified Zhang et al. models:

$$I_{Ca,L} = g_{Ca,L} \times \{1 - 0.0037 \times [ACh]/(0.007 \times [ACh] + 0.0000006)\} \times (V - 46.4) \times (d_L \times f_L + 0.006/\{1 + \exp[-(V + 14.1)/6]\}) \quad (A8)$$

$g_{Ca,L}$=0.2752(central) or 0.9630 (peripheral)

$$d_{L\infty} = \{1 + \exp[-(V + 22.3 + 0.8 \times F_{Cell} - 5)/6]\}^{-1} \quad (A9)$$

$$f_{L\infty} = \{1 + \exp[(V + 45 - 10)/5]\}^{-1} \quad (A10)$$

$$\tau_{dL} = 2000 \times (\alpha_{dL} + \beta_{dL})^{-1} \quad (A11)$$

$$\alpha_{dL} = -28.39 \times (V + 35)/\{\exp[-(V + 35)/2.5] - 1\} - 84.9 \times V/\{\exp[-0.208 \times V] - 1\} \quad (A12)$$

$$\beta_{dL} = 11.43 \times (V - 5)/\{\exp[0.4 \times (V - 5)] - 1\} \quad (A13)$$

$$\tau_{fL} = 1000 \times (1.2 - 0.2 \times F_{Cell}) \times (\alpha_{fL} + \beta_{fL})^{-1} \quad (A14)$$

$$\alpha_{fL} = 3.75 \times (V + 28)/\{\exp[(V + 28)/4] - 1\} \quad (A15)$$

$$\beta_{fL} = 30/\{1 + \exp[-(V + 28)/4]\} \quad (A16)$$

$$F_{Cell} = 1.0309347 \times d_{Cell}/\{1 + 0.7745 \times \exp[-(3 \times d_{Cell} - 2.05)/0.295]\} \quad (A17)$$

$$d_{Cell} = 0 \text{ (central) or } 1 \text{ (peripheral)}.$$

L-type Ca^{2+} channel current ($I_{Ca,L}$) for Kurata et al. models:

$$I_{Ca,L} = g_{Ca,L} \times \{1 - 0.0037 \times [ACh]/(0.007 \times [ACh] + 0.0000006)\} \times (V - 45) \times d_L \times f_L \times f_{Ca} \quad (A18)$$

$$d_{L\infty} = \{1 + \exp[-(V + 14.1)/6]\}^{-1} \quad \text{(A19)}$$

$$f_{L\infty} = \{1 + \exp[(V + 30)/5]\}^{-1} \quad \text{(A20)}$$

$$f_{Ca\infty} = 0.00035/(0.00035 + [Ca^{2+}]_{sub}) \quad \text{(A21)}$$

$$\tau_{dL} = (\alpha_{dL} + \beta_{dL})^{-1} \quad \text{(A22)}$$

$$\alpha_{dL} = -0.02839 \times (V + 35)/\{\exp[-(V + 35)/2.5] - 1\} - 0.0849 \times V/\{\exp[-V/4.808] - 1\} \quad \text{(A23)}$$

$$\beta_{dL} = 0.01143 \times (V - 5)/\{\exp[(V - 5)/2.5] - 1\} \quad \text{(A24)}$$

$$\tau_{fL} = 257.1 \times \exp[-(V + 32.5)^2/13.9^2] + 44.3 \quad \text{(A25)}$$

$$\tau_{fCa} = 1/(0.021 + 60 \times [Ca^{2+}]_{sub}). \quad \text{(A26)}$$

Hyperpolarization-activated cation current (I_h):

$$I_h = [g_{h,Na} \times (V - E_{Na}) + g_{h,K} \times (V - E_K)] \times y \quad \text{(A27)}$$

$$y_\infty = \alpha_y/(\alpha_y + \beta_y) \quad \text{(A28)}$$

$$\tau_{dL} = 1000 \times (\alpha_y + \beta_y)^{-1} \quad \text{(A29)}$$

$$\alpha_y = \exp[-(V + 78.91 - dV_y)/26.63] \quad \text{(A30)}$$

$$\beta_y = \exp[(V + 75.13 - dV_y)/21.25] \quad \text{(A31)}$$

$$dV_y = -10 \times \{[ACh]/([ACh] + 0.0000025)\}^4. \quad \text{(A32)}$$

Muscarinic K^+ channel current ($I_{K,ACh}$):

$$I_{K,ACh} = 0.031 \times [K^+]_o^{0.41} \times \{[ACh]/([ACh] + 0.000057447)\}^4 \times \{[K^+]_I - [K^+]_o \times \exp(-V \times F/RT)\}. \quad \text{(A33)}$$

APPENDIX B: STABILITY ANALYSIS BASED ON THE LINEAR STABILITY THEORY

We evaluated the stability of EPs according to the linear stability theory, i.e., by linear approximation of a nonlinear system at an EP (see (71,72)). For simplicity, first consider the two-dimensional autonomous system of the form

$$dx_1/dt = f_1(x_1, x_2), \quad dx_2/dt = f_2(x_1, x_2), \quad \text{(A34a)}$$

or the vector form

$$d\mathbf{x}/dt = \mathbf{f}(\mathbf{x}), \mathbf{x} = (x_1, x_2)^T, \quad \mathbf{f}(\mathbf{x}) = [f_1(x_1, x_2), f_2(x_1, x_2)]^T \quad \text{(A34b)}$$

(T denotes transpose). Suppose that the EP to be (x_{1E}, x_{2E}), so that $f_1(x_{1E}, x_{2E}) = f_2(x_{1E}, x_{2E}) = 0$. We can therefore write, by a Taylor series expansion of the vector field $f_i(x_1, x_2)$ around the EP,

$$f_1(x_1, x_2) = \partial f_1/\partial x_1(x_{1E}, x_{2E}) \times (x_1 - x_{1E}) + \partial f_1/\partial x_2(x_{1E}, x_{2E}) \times (x_2 - x_{2E}) + O(\text{tho}),$$
$$f_2(x_1, x_2) = \partial f_2/\partial x_1(x_{1E}, x_{2E}) \times (x_1 - x_{1E}) + \partial f_2/\partial x_2(x_{1E}, x_{2E}) \times (x_2 - x_{2E}) + O(\text{tho}), \quad \text{(A35)}$$

where the symbol O stands for the term of higher order (tho). Thus, the linear approximation to Eq. A34 in the neighborhood of the EP is defined as the system for $h_1(= x_1\text{-}x_{1E})$ and $h_2(= x_2\text{-}x_{2E})$:

$$dh_1/dt = \partial f_1/\partial x_1(x_{1E}, x_{2E}) \times h_1 + \partial f_1/\partial x_2(x_{1E}, x_{2E}) \times h_2,$$
$$dh_2/dt = \partial f_2/\partial x_1(x_{1E}, x_{2E}) \times h_1 + \partial f_2/\partial x_2(x_{1E}, x_{2E}) \times h_2. \quad \text{(A36a)}$$

This linearized system is also written in the vector form

$$d\mathbf{h}/dt = \mathbf{Df}(\mathbf{x_E}) \times \mathbf{h}, \mathbf{h} = (h_1, h_2)^T,$$
$$d\mathbf{h}/dt = [dh_1/dt, dh_2/dt]^T, \quad \text{(A36b)}$$

where $\mathbf{Df}(\mathbf{x_E})$ is the Jacobian matrix of first-order partial derivatives of $\mathbf{f}(\mathbf{x})$, denoted by:

$$\mathbf{Df}(\mathbf{x_E}) = \begin{bmatrix} \partial f_1/\partial x_1(x_{1E}, x_{2E}), \partial f_1/\partial x_2(x_{1E}, x_{2E}) \\ \partial f_2/\partial x_1(x_{1E}, x_{2E}), \partial f_2/\partial x_2(x_{1E}, x_{2E}) \end{bmatrix} \quad \text{(A37)}$$

We can expect in most cases that the solutions of Eq. A36 will be geometrically similar to those of Eq. A34 near the EP. It is well known that there are solutions of Eq. A36 of the form

$$h_1(t) = C_1 \times r_{11} \times \exp(\lambda_1 \times t) + C_2 \times r_{12} \times \exp(\lambda_2 \times t),$$
$$h_2(t) = C_1 \times r_{21} \times \exp(\lambda_1 \times t) + C_2 \times r_{22} \times \exp(\lambda_2 \times t), \quad \text{(A38a)}$$

or the vector form

$$\mathbf{h}(t) = C_1 \times \mathbf{r}_1 \times \exp(\lambda_1 \times t) + C_2 \times \mathbf{r}_2 \times \exp(\lambda_2 \times t),$$
$$\mathbf{h}(t) = [h_1(t), h_2(t)]^T, \quad \mathbf{r}_1 = (r_{11}, r_{21})^T, \quad \mathbf{r}_2 = (r_{12}, r_{22})^T, \quad \text{(A38b)}$$

where λ_1 and λ_2 are the eigenvalues (roots of the characteristic equation) for the Jacobian matrix $\mathbf{Df(x_E)}$. C_1 and C_2 are arbitrary constants to be complex in general. The approximation $\mathbf{h}(t)$ describes the local behavior of the solution, indicating how the process evolves when the initial state deviates slightly from the EP. When λ_i is complex, represented as

$$\lambda_I = \text{Re}[\lambda_i] + j \times \text{Im}[\lambda_i], \quad \text{(A39)}$$

we obtain

$$h_1(t) = \sum C_i \times r_{1i} \times \exp(\text{Re}[\lambda_i] \times t) \times [\cos(\text{Im}[\lambda_i] \times t) + j \times \sin(\text{Im}[\lambda_i] \times t)],$$
$$h_2(t) = \sum C_i \times r_{2i} \times \exp(\text{Re}[\lambda_i] \times t) \times [\cos(\text{Im}[\lambda_i] \times t) + j \times \sin(\text{Im}[\lambda_i] \times t)] (i = 1, 2). \quad \text{(A40)}$$

Here $\text{Re}[\lambda_i]$ and $\text{Im}[\lambda_i]$ are respectively the real and imaginary part of λ_i. For a more general case of an n-dimensional autonomous system of the form

$$d\mathbf{x}/dt = \mathbf{f}(\mathbf{x}), \mathbf{x} = (x_1, x_2, \ldots, x_n)^T, \mathbf{f}(\mathbf{x}) = [f_1(x_1, x_2, \ldots, x_n), f_2(x_1, x_2, \ldots, x_n), \ldots, f_n(x_1, x_2, \ldots, x_n)]^T, \quad \text{(A41)}$$

the linearized form around an EP of $\mathbf{x}_E = (x_{1E}, x_{2E}, \ldots, x_{nE})^T$ is

$$d\mathbf{h}/dt = \mathbf{Df}(\mathbf{x_E}) \times \mathbf{h}, \quad \mathbf{h} = (h_1, h_2, \ldots, h_n)^T,$$
$$d\mathbf{h}/dt = [dh_1/dt, dh_2/dt, \ldots, dh_n/dt]^T. \quad \text{(A42)}$$

Then, the solution of Eq. A42 is given by

$$\mathbf{h}(t) = [h_1(t), h_2(t), \ldots, h_k(t), \ldots, h_n(t)]^T,$$
$$h_k(t) = \sum C_i \times r_{ki} \times \exp(\lambda_i \times t) = \sum C_i \times r_{ki} \times \exp(\mathrm{Re}[\lambda_i] \times t) \times [\cos(\mathrm{Im}[\lambda_i] \times t) + j \times \sin(\mathrm{Im}[\lambda_i] \times t)](i,k = 1,2,\ldots,n). \quad \text{(A43)}$$

Thus, $\mathrm{Re}[\lambda_i]$ represents the rate constant of a solution beneath the EP to be attracted to or go away from the EP. The EP is stable if all of the $\mathrm{Re}[\lambda_i]$ values are negative because the system is asymptotically attracted to the EP; it is unstable if at least one of $\mathrm{Re}[\lambda_i]$ values is positive because the system goes away from the EP.

APPENDIX C: CONSTRUCTION OF TWO-PARAMETER BIFURCATION DIAGRAMS FOR $G_{CA,L}$ AND G_{NA}

The two-parameter bifurcation diagrams for $g_{Ca,L}$ and g_{Na} (Fig. 15) show how the stability of EPs reverses via Hopf bifurcations during the inhibition of $I_{Ca,L}$ and/or I_{Na}. One-parameter bifurcation diagrams for $g_{Ca,L}$ of 0–1 were first constructed with various g_{Na} values of 0–1 (with intervals of 0.001) by the stability analysis for EPs; those for $g_{Na} = 1$, 0.9, 0.8, 0.7, 0.65, 0.6, 0.4, 0.2, and 0 are shown in Fig. 18 (*top-right*). To construct the two-parameter bifurcation diagrams as shown in Fig. 15, the critical $g_{Ca,L}$ values at Hopf bifurcations in the one-parameter bifurcation diagrams were plotted as functions of g_{Na} (Fig. 18 *top-left*). This two-parameter bifurcation diagram can also be constructed from one-parameter bifurcation diagrams for g_{Na} determined with various $g_{Ca,L}$ values (see Fig. 18 *bottom* for $g_{Ca,L} = 1$, 0.9, 0.8, 0.7, 0.6, 0.5, 0.4, 0.2, and 0).

This work was supported in part by the Ministry for Education, Science, Sports and Culture of Japan Grant-in-Aid for Scientific Research (C) 17590192 (to Y.K. and T.S.), Kanazawa Medical University Grant for Collaborative Research C2005-1 (to Y.K. and T.S.), and Kanazawa Medical University Grant for Promoted Research S2006-6 and S2007-2 (to Y.K.).

REFERENCES

1. Noma, A. 1996. Ionic mechanisms of the cardiac pacemaker potential. *Jpn. Heart J.* 37:673–682.
2. Kurata, Y., I. Hisatome, S. Imanishi, and T. Shibamoto. 2003. Roles of L-type Ca^{2+} and delayed-rectifier K^+ currents in sinoatrial node pacemaking: insights from stability and bifurcation analyses of a mathematical model. *Am. J. Physiol. Heart Circ. Physiol.* 285:H2804–H2819.
3. Kodama, I., M. R. Nikmaram, M. R. Boyett, R. Suzuki, H. Honjo, and J. M. Owen. 1997. Regional differences in the role of the Ca^{2+} and Na^+ currents in pacemaker activity in the sinoatrial node. *Am. J. Physiol. Heart Circ. Physiol.* 272:H2793–H2806.
4. Kreitner, D. 1985. Electrophysiological study of the two main pacemaker mechanisms in the rabbit sinus node. *Cardiovasc. Res.* 19:304–318.
5. Zhang, H., and M. Vassalle. 2000. Role of dual pacemaker mechanisms in sinoatrial node discharge. *J. Biomed. Sci.* 7:100–113.
6. Zhang, H., and M. Vassalle. 2001. Role of I_K and I_f in the pacemaker mechanisms of sino-atrial node myocytes. *Can. J. Physiol. Pharmacol.* 79:963–976.
7. Chay, T. R., and Y. S. Lee. 1985. Phase resetting and bifurcation in the ventricular myocardium. *Biophys. J.* 47:641–651.
8. Chay, T. R., and Y. S. Lee. 1990. Bursting, beating, and chaos by two functionally distinct inward current inactivations in excitable cells. *Ann. N. Y. Acad. Sci.* 591:328–350.
9. Guevara, M. R., and H. J. Jongsma. 1992. Three ways of abolishing automaticity in sinoatrial node: ionic modeling and nonlinear dynamics. *Am. J. Physiol.* 262:H1268–H1286.
10. Landau, M., P. Lorente, D. Michaels, and J. Jalife. 1990. Bistabilities and annihilation phenomena in electrophysiological cardiac models. *Circ. Res.* 66:1658–1672.
11. Varghese, A., and R. L. Winslow. 1994. Dynamics of abnormal pacemaking activity in cardiac Purkinje fibers. *J. Theor. Biol.* 168:407–420.
12. Vinet, A., and F. A. Roberge. 1990. A model study of stability and oscillations in the myocardial cell membrane. *J. Theor. Biol.* 147: 377–412.
13. Kurata, Y., I. Hisatome, H. Matsuda, and T. Shibamoto. 2005. Dynamical mechanisms of pacemaker generation in I_{K1}-downregulated human ventricular myocytes: Insights from bifurcation analyses of a mathematical model. *Biophys. J.* 89: 2865–2887.
14. Kurata, Y., I. Hisatome, S. Imanishi, and T. Shibamoto. 2002. Dynamical description of sinoatrial node pacemaking: improved mathematical model for primary pacemaker cell. *Am. J. Physiol. Heart Circ. Physiol.* 283:H2074–H2101.
15. Zhang, H., A. V. Holden, I. Kodama, H. Honjo, M. Lei, T. Varghese, and M. R. Boyett. 2000. Mathematical models of action potentials in the periphery and center of the rabbit sinoatrial node. *Am. J. Physiol. Heart Circ. Physiol.* 279:H397–H421.
16. Garny, A., P. Kohl, P. J. Hunter, M. R. Boyett, and D. Noble. 2003. One-dimensional rabbit sinoatrial node models: benefits and limitations. *J. Cardiovasc. Electrophysiol.* 14:S121–S132.
17. Gepstein, L., Y. Feld, and L. Yankelson. 2004. Somatic gene and cell therapy strategies for the treatment of cardiac arrhythmias. *Am. J. Physiol. Heart Circ. Physiol.* 286:815–822.
18. Kurata, Y., H. Matsuda, I. Hisatome, and T. Shibamoto. 2007. Effects of pacemaker currents on creation and modulation of human ventricular pacemaker: theoretical study with application to biological pacemaker engineering. *Am. J. Physiol. Heart Circ. Physiol.* 292: H701–H718.
19. Guckenheimer, J., and P. Holmes. 1983. Nonlinear Oscillations, Dynamical Systems, and Bifurcations of Vector Fields. Springer-Verlag, New York.
20. Parker, T. S., and L. O. Chua. 1989. Practical Numerical Algorithms for Chaotic Systems. Springer-Verlag, New York.
21. Kuznetsov, Y. A. 2003. Elements of Applied Bifurcation Theory, 3rd edition. Springer-Verlag, New York.
22. Zhang, H., Y. Zhao, M. Lei, H. Dobrzynski, J. H. Liu, A. V. Holden, and M. R. Boyett. 2007. Computational evaluation of the roles of Na^+ current, I_{Na}, and cell death in cardiac pacemaking and driving. *Am. J. Physiol. Heart Circ. Physiol.* 292:H165–H174.
23. Wilders, R., H. J. Jongsma, and A. C. G. van Ginneken. 1991. Pacemaker activity of the rabbit sinoatrial node: a comparison of mathematical models. *Biophys. J.* 60:1202–1216.
24. Demir, S. S., J. W. Clark, C. R. Murphey, and W. R. Giles. 1994. A mathematical model of a rabbit sinoatrial node cell. *Am. J. Physiol.* 266:C832–C852.
25. Dokos, S., B. Celler, and N. Lovell. 1996. Ion currents underlying sinoatrial node pacemaker activity: a new single cell mathematical model. *J. Theor. Biol.* 181:245–272.
26. Sarai, N., S. Matsuoka, S. Kuratomi, K. Ono, and A. Noma. 2003. Role of individual ionic current systems in the SA node hypothesized by a model study. *Jpn. J. Physiol.* 53:125–134.
27. Baruscotti, M., D. DiFrancesco, and R. B. Robinson. 1996. A TTX-sensitive inward sodium current contributes to spontaneous activity in newborn rabbit sino-atrial node cells. *J. Physiol.* 492:21–30.
28. Muramatsu, H., A.-R. Zou, G. A. Berkowitz, and R. D. Nathan. 1996. Characterization of a TTX-sensitive Na^+ current in pacemaker cells isolated from rabbit sinoatrial node. *Am. J. Physiol.* 270:H2108–H2119.
29. Dokos, S., B. G. Celler, and N. H. Lovell. 1996. Vagal control of sinoatrial rhythm: a mathematical model. *J. Theor. Biol.* 182:21–44.
30. Zhang, H., A. V. Holden, D. Noble, and M. R. Boyett. 2002. Analysis of the chronotropic effect of acetylcholine on sinoatrial node cells. *J. Cardiovasc. Electrophysiol.* 13:465–474.

31. Beau, S. L., D. E. Hand, R. B. Schuessler, B. I. Bromberg, B. Kwon, J. P. Boineau, and J. E. Saffitz. 1995. Relative densities of muscarinic cholinergic and beta-adrenergic receptors in the canine sinoatrial node and their relation to sites of pacemaker activity. *Circ. Res.* 77:957–963.

32. Roberts, L. A., G. R. Slocum, and D. A. Riley. 1989. Morphological study of the innervation pattern of the rabbit sinoatrial node. *Am. J. Anat.* 185:74–88.

33. Watanabe, E. I., H. Honjo, T. Anno, M. R. Boyett, I. Kodama, and J. Toyama. 1995. Modulation of pacemaker activity of sinoatrial node cells by electrical load imposed by an atrial cell model. *Am. J. Physiol. Heart Circ. Physiol.* 269:H1735–H1742.

34. Dhooge, A., W. Govaerts, Yu. A. Kuznetsov, W. Mestrom, A. M. Riet, and B. Sautois. 2006. MATCONT and CL_MATCONT: Continuation Toolboxes in MATLAB. http://www.matcont.ugent.be/matcont.html.

35. Fukai, H., S. Doi, T. Nomura, and S. Sato. 2000. Hopf bifurcations in multiple-parameter space of the Hodgkin-Huxley equations I. Global organization of bistable periodic solutions. *Biol. Cybern.* 82:215–222.

36. Boyett, M. R., H. Honjo, and I. Kodama. 2000. The sinoatrial node, a heterogeneous pacemaker structure. *Cardiovasc. Res.* 47:658–687.

37. Shibata, N., S. Inada, K. Mitsui, H. Honjo, M. Yamamoto, R. Niwa, M. R. Boyett, and I. Kodama. 2001. Pacemaker shift in the rabbit sinoatrial node in response to vagal nerve stimulation. *Exp. Physiol.* 86:177–184.

38. Lancaster, M. K., S. A. Jones, S. M. Harrison, and M. R. Boyett. 2004. Intracellular Ca^{2+} and pacemaking within the rabbit sinoatrial node: heterogeneity of role and control. *J. Physiol.* 556:481–494.

39. Musa, H., M. Lei, H. Honjo, S. A. Jones, H. Dobrzynski, M. K. Lancaster, Y. Takagishi, Z. Henderson, I. Kodama, and M. R. Boyett. 2002. Heterogeneous expression of Ca^{2+} handling proteins in rabbit sinoatrial node. *J. Histochem. Cytochem.* 50:311–324.

40. Boyett, M. R., H. Zhang, A. Garny, and A. V. Holden. 2001. Control of the pacemaker activity of the sinoatrial node by intracellular Ca^{2+}. Experiments and modelling. *Philos. Trans. R. Soc. Lond. A Math. Phys. Sci.* 359:1091–1110.

41. Lei, M., S. A. Jones, J. Liu, M. K. Lancaster, S. S.-M. Fung, H. Dobrzynski, P. Camelliti, S. K. G. Maier, D. Noble, and M. R. Boyett. 2004. Requirement of neuronal- and cardiac-type sodium channels for murine sinoatrial node pacemaking. *J. Physiol.* 559:835–848.

42. Lei, M., C. Goddard, J. Liu, A. L. Leoni, A. Royer, S. S. Fung, G. Xiao, A. Ma, H. Zhang, F. Charpentier, J. I. Vandenberg, W. H. Colledge, A. A. Grace, and C. L. Huang. 2005. Sinus node dysfunction following targeted disruption of the murine cardiac sodium channel gene Scn5a. *J. Physiol.* 567:387–400.

43. Benson, D. W., D. W. Wang, M. Dyment, T. K. Knilans, F. A. Fish, M. J. Strieper, T. H. Rhodes, and A. L. George, Jr. 2003. Congenital sick sinus syndrome caused by recessive mutations in the cardiac sodium channel gene (SCN5A). *J. Clin. Invest.* 112:1019–1028.

44. Smits, J. P., T. T. Koopmann, R. Wilders, M. W. Veldkamp, T. Opthof, Z. A. Bhuiyan, M. M. Mannens, J. R. Balser, H. L. Tan, C. R. Bezzina, and A. A. Wilde. 2005. A mutation in the human cardiac sodium channel (E161K) contributes to sick sinus syndrome, conduction disease and Brugada syndrome in two families. *J. Mol. Cell. Cardiol.* 38:969–981.

45. Satin, J., I. Kehat, O. Caspi, I. Huber, G. Arbel, I. Itzhaki, J. Magyar, E. A. Schroder, I. Perlman, and L. Gepstein. 2004. Mechanisms of spontaneous excitability in human embryonic stem cell derived cardiomyocytes. *J. Physiol.* 559:479–496.

46. Gibb, W. J., M. B. Wagner, and M. D. Lesh. 1994. Effects of simulated potassium blockade on the dynamics of triggered cardiac activity. *J. Theor. Biol.* 168:245–257.

47. Miake, J., E. Marbán, and H. B. Nuss. 2002. Gene therapy: biological pacemaker created by gene transfer. *Nature.* 419:132–133.

48. Qu, J., A. N. Plotnikov, P. Danilo, Jr., I. Shlapakova, I. S. Cohen, R. B. Robinson, and M. R. Rosen. 2003. Expression and function of a biological pacemaker in canine heart. *Circulation.* 107:1106–1109.

49. Plotnikov, A. N., E. A. Sosunov, J. Qu, I. N. Shlapakova, E. P. Anyukhovsky, L. Liu, M. J. Janse, P. R. Brink, I. S. Cohen, R. B. Robinson, P. Danilo, Jr., and M. R. Rosen. 2004. Biological pacemaker implanted in canine left bundle branch provides ventricular escape rhythms that have physiologically acceptable rates. *Circulation.* 109: 506–512.

50. He, J.-Q., Y. Ma, Y. Lee, J. A. Thomson, and T. J. Kamp. 2003. Human embryonic stem cells develop into multiple types of cardiac myocytes: action potential characterization. *Circ. Res.* 93:32–39.

51. Xue, T., H. C. Cho, F. G. Akar, S.-Y. Tsang, S. P. Jones, E. Marbán, G. F. Tomaselli, and R. A. Li. 2005. Functional integration of electrically active cardiac derivatives from genetically engineered human embryonic stem cells with quiescent recipient ventricular cardiomyocytes: insights into the development of cell-based pacemakers. *Circulation.* 111:11–20.

52. Demir, S. S., J. W. Clark, and W. R. Giles. 1999. Parasympathetic modulation of sinoatrial node pacemaker activity in rabbit heart: a unifying model. *Am. J. Physiol.* 276:H2221–H2244.

53. Greenstein, J. L., and R. L. Winslow. 2002. An integrative model of the cardiac ventricular myocytes incorporating local control of Ca^{2+} release. *Biophys. J.* 83:2918–2945.

54. Saucerman, J. J., L. L. Brunton, A. P. Michailova, and A. D. McCulloch. 2003. Modeling β-adrenergic control of cardiac myocytes contractility *in silico*. *J. Biol. Chem.* 278:47997–48003.

55. Shannon, T. R., F. Wang, J. Puglisi, C. Weber, and D. M. Bers. 2004. A mathematical treatment of integrated Ca dynamics within the ventricular myocyte. *Biophys. J.* 87:3351–3371.

56. Clancy, C. E., and Y. Rudy. 1999. Linking a genetic defect to its cellular phenotype in a cardiac arrhythmia. *Nature.* 400:566–569.

57. Irvine, L. A., M. S. Jafri, and R. L. Winslow. 1999. Cardiac sodium channel Markov model with temperature dependence and recovery from inactivation. *Biophys. J.* 76:1868–1885.

58. Iyer, V., R. Mazhari, and R. L. Winslow. 2004. A computational model of the human left-ventricular epicardial myocyte. *Biophys. J.* 87:1507–1525.

59. Lakatta, E. G., V. A. Maltsev, K. Y. Bogdanov, M. D. Stern, and T. M. Vinogradova. 2003. Cyclic variation of intracellular calcium: a critical factor for cardiac pacemaker cell dominance. *Circ. Res.* 92: e45–e50.

60. Vinogradova, T. M., Y.-Y. Zhou, V. A. Maltsev, A. E. Lyashkov, M. Stern, and E. G. Lakatta. 2004. Rhythmic ryanodine receptor Ca^{2+} releases during diastolic depolarization of sinoatrial pacemaker cells do not require membrane depolarization. *Circ. Res.* 94:802–809.

61. Vinogradova, T. M., V. A. Maltsev, K. Y. Bogdanov, A. E. Lyashkov, and E. G. Lakatta. 2005. Rhythmic Ca^{2+} oscillations drive sinoatrial nodal cell pacemaker function to make the heart tick. *Ann. N. Y. Acad. Sci.* 1047:138–156.

62. Lakatta, E. G., T. M. Vinogradova, A. Lyashkov, S. Sirenko, W. Zhu, A. Ruknudin, and V. A. Maltsev. 2006. The integration of spontaneous intracellular Ca^{2+} cycling and surface membrane ion channel activation entrains normal automaticity in cells of the heart's pacemaker. *Ann. N. Y. Acad. Sci.* 1080:178–206.

63. Maltsev, V. A., T. M. Vinogradova, and E. G. Lakatta. 2006. The emergence of a general theory of the initiation and strength of the heartbeat. *J. Pharmacol. Sci.* 100:338–369.

64. Li, J., J. Qu, and R. D. Nathan. 1997. Ionic basis of ryanodine's negative chronotropic effect on pacemaker cells isolated from the sinoatrial node. *Am. J. Physiol.* 273:H2481–H2489.

65. Honjo, H., S. Inada, M. K. Lancaster, M. Yamamoto, R. Niwa, S. A. Jones, N. Shibata, K. Mitsui, T. Horiuchi, K. Kamiya, I. Kodama, and M. R. Boyett. 2003. Sarcoplasmic reticulum Ca^{2+} release is not a dominating factor in sinoatrial node pacemaker activity. *Circ. Res.* 92:e41–e44.

66. Maltsev, V. A., T. M. Vinogradova, K. Y. Bogdanov, E. G. Lakatta, and M. D. Stern. 2004. Diastolic calcium release controls the beating

rate of rabbit sinoatrial node cells: numerical modeling of the coupling process. *Biophys. J.* 86:2596–2605.

67. Boyett, M. R., H. Dobrzynski, M. K. Lancaster, S. A. Jones, H. Honjo, and I. Kodama. 2003. Sophisticated architecture is required for the sinoatrial node to perform its normal pacemaker function. *J. Cardiovasc. Electrophysiol.* 14:104–106.
68. Joyner, R. W., Y.-G. Wang, R. Wilders, D. A. Golod, M. B. Wagner, R. Kumar, and W. N. Goolsby. 2000. A spontaneously active focus drives a model atrial sheet more easily than a model ventricular sheet. *Am. J. Physiol. Heart Circ. Physiol.* 279:H752–H763.
69. Verheijck, E. E., R. Wilders, and L. N. Bouman. 2002. Atrio-sinus interaction demonstrated by blockade of the rapid delayed rectifier current. *Circulation.* 105:880–885.
70. Michaels, D. C., E. P. Matyas, and J. Jalife. 1987. Mechanisms of sinoatrial pacemaker synchronization: a new hypothesis. *Circ. Res.* 61:704–714.
71. Jordan, D. W., and P. Smith. 1987. Nonlinear Ordinary Differential Equations, 2nd edition. Oxford University Press, New York.
72. Seydel, R. 1994. Practical Bifurcation and Stability Analysis: From Equilibrium to Chaos, 2nd edition. Springer-Verlag, New York.